ISSN 1063-7842, Technical Physics, 2013, Vol. 58, No. 1, pp. 1–24. © Pleiades Publishing, Ltd., 2013.
Original Russian Text © I.B. Vendik, O.G. Vendik, 2013, published in Zhurnal Tekhnicheskoi Fiziki, 2013, Vol. 83, No. 1, pp. 3–28.

Metamaterials and Their Application in Microwaves: A Review

I. B. Vendik* and O. G. Vendik**

St. Petersburg Electrotechnical University "LETI," ul. Prof. Popova 5, St. Petersburg, 197376 Russia
**e-mail: ibvendik@rambler.ru*
***e-mail: ogvendik@rambler.ru*

Received June 28, 2012

Abstract—A metamaterial is a composite material that has attracted the attention of researchers since the late 1990s–early 2000s. This material contains an artificial periodic structure, which modifies its permittivity and permeability and, thereby, makes it possible to control the dispersion, refraction, and reflection of electromagnetic waves in the metamaterial. Analytical and experimental studies of the properties of metamaterials, as well as their applications, cover a wide frequency range from radio waves to the visible range. In recent years, considerable progress has been made toward the application of these materials in the microwave range (1–100 GHz). Works on development and application of metamaterials in the microwave range published over the last 8–10 years are reviewed. Artificial transmission lines as 1D metamaterials are discussed. Resonators, filters, and phase shifters based on the "metamaterial philosophy" are considered. Special attention is given to the application of metamaterials in the antenna technology.

DOI: 10.1134/S1063784213010234

INTRODUCTION

A metamaterial is a composite the properties of which depend rather on an artificial periodic structure made up of macroscopic elements with arbitrary sizes and shapes than on the properties of its constituents. In a very rough approximation, these macroelements can be viewed as very large atoms embedded in a host material (matrix). The artificial periodic structure modifies the permittivity and permeability of the matrix, so that designers of metamaterials can control a number of free parameters (such as the size and shape of the structure and the constant and variable lattice parameters of the constituents). Metamaterials may have a negative refractivity, which shows up when both the permittivity and the permeability of the material are negative.

Interest in negative-refractivity materials dates back to 1967, when a work of Soviet physicist Veselago was published [1]. He demonstrated the feasibility of negative-refractivity materials, which were named "the left-handed materials" (it would be then well to name positive-refractivity materials "right-handed materials" by analogy). Veselago concluded that all known optical laws of wave propagation in such materials change significantly, although negative-refractivity materials were not known at that time. It should be noted, however, that actually such left-handed media were discussed well before, in 1957–1960, by Pafomov [2], Sivukhin [3], and Silin [4] (for a more detailed description of the background of the problem, see review [5] of Agranovich and Gartshtein). Relevant information is also contained in reviews devoted to the propagation of electromagnetic waves in metamaterials and the feasibility of their application in various fields of technology [6, 7]. A two-volume book of more than one thousand pages in it [8] is also worth noting. This book is an international symposium on the physics and application of metamaterials, and symposiasts are researchers working worldwide, including at Russian scientific centers. Of particular interest here are monographs [9–12], where the physics and technical applications of metamaterials are described at length.

1. BASIC PROPERTIES OF METAMATERIALS

In his seminal work, Veselago showed that the pattern of refraction—deflection of an electromagnetic wave when passing through the interface between two media—varies depending on whether the refractivities of both materials are of the same or opposite sign. If the refractivities of the materials are of the same sign, the wave incident on the interface on one side of the normal to it appears, after being refracted, on the other side of the normal. If the refractivities of the materials are of opposite sign, the incident and refracted waves are on the same side of the normal.

Another intriguing property of metamaterials is the specific dispersion of waves propagating in them. The equation of electromagnetic wave propagation in an isotropic medium has the form

$$k^2 - (\omega/c)^2 n^2 = 0, \quad (1)$$

where k is the wavenumber; ω is the angular frequency of the wave; c is the velocity of light in vacuum; $n_2 = \varepsilon\mu$

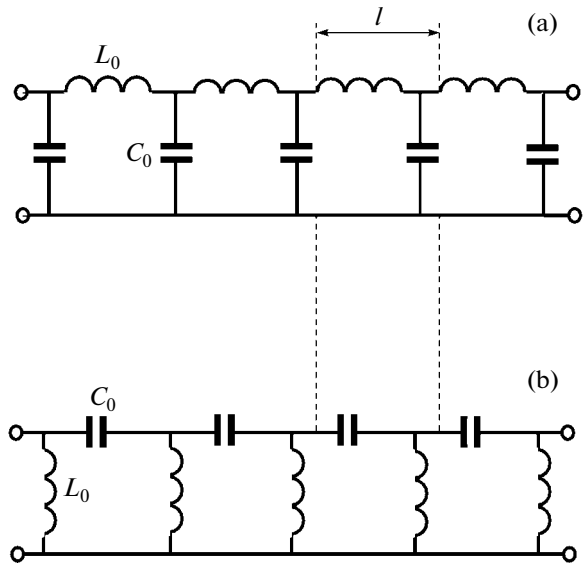

Fig. 1. (a) Right-handed and (b) left-handed artificial transmission lines with lumped capacitances and inductances.

is the refractive index squared; and ε and μ are, respectively, the permittivity and permeability of the medium. The term "dispersion" signifies the dependence of the wave oscillation frequency on the wavenumber or, in other words, on wavelength λ ($k = 2\pi/\lambda$) of the oscillatory process. From (1) we have

$$\omega = \frac{c}{n}k. \tag{2}$$

The dispersion of an electromagnetic wave depends primarily on the refractive index. Left-handed media have a negative refractive index.

Equation (1) was derived from the Maxwell theory. For media in which both permittivity ε and permeability μ are positive, electric vector **E**, magnetic vector **H**, and propagation vector **k** of the electromagnetic field produce a so-called right-handed system of vectors,

$$\begin{aligned}[\mathbf{kE}] &= (\omega/c)\mu\mathbf{H},\\ [\mathbf{kH}] &= -(\omega/c)\varepsilon\mathbf{E}.\end{aligned} \tag{3}$$

Such media are referred to as "right-handed media."

For media in which both ε and μ are negative, electric vector **E**, magnetic vector **H**, and propagation vector **k** produce a left-handed system of vectors. The respective materials are called right- and left-handed materials.

To characterize the propagation and dispersion of waves, it is necessary to give a definition of the phase and group velocities of a wave. For a plane harmonic wave, the phase velocity in the direction of the propagation vector is the velocity of the equiphase surface, which can be expressed as follows:

$$v_{\mathrm{ph}} = \frac{\omega}{k}. \tag{4}$$

Substituting expression (2) for ω into (4) yields the seemingly obvious relationship

$$v_{\mathrm{ph}} = \frac{c}{n}, \tag{5}$$

from which it follows that the phase velocity of a wave in a metamaterial can be negative. The negativeness of the phase velocity means that, when a wave propagates, the phase advances from the detector to the source, whereas the energy is obviously transferred in the reverse direction.

The group velocity characterizes the propagation velocity of a "group of waves" or, in other words, a more or less localized quasi-monochromatic wave (wave with a narrow spectrum). The group velocity is usually treated as the propagation velocity of the maximum of the amplitude envelope of a quasi-monochromatic wave packet. In the 1D case, the group velocity is determined from the dispersion law,

$$v_{\mathrm{gr}} = \frac{d\omega}{dk}. \tag{6}$$

If the dispersion properties of the medium are such that the wave packet propagates without significantly changing the shape of its envelope, the group velocity can be viewed as the transfer rate of the wave "energy" or the rate with which the wave packet transfers information-bearing signals in accordance with the causality principle. As follows from the relativity theory, the group velocity is always positive and is lower than, or equal to, the velocity of light in vacuum. In 1D dispersion-free media, the group velocity coincides with the phase velocity.

The dispersion of waves in left- and right-handed materials is illustrated with a simple example. Figure 1 shows two artificial transmission lines made up of lumped capacitances and inductances. The dispersion laws in these transmission lines are different.

For the right-handed transmission line, we have

$$\omega = \frac{k}{\sqrt{L_1 C_1}}, \tag{7}$$

where $L_1 = L_0/l$ is the inductance per unit length of conductors in the line and $C_1 = C_0/l$ is the capacitance per unit length between the conductors.

For the left-handed line, we have

$$\omega = -\frac{1}{k\sqrt{\left(\frac{1}{L}\right)_1\left(\frac{1}{C}\right)_1}}, \tag{8}$$

where $\left(\frac{1}{L}\right)_1$ is the inverse inductance per unit length between the conductors in the transmission line and $\left(\frac{1}{C}\right)_1$ is the inverse capacitance per unit length series-connected to the conductors.

It should be emphasized that the left-handed lumped-element transmission line is artificial,

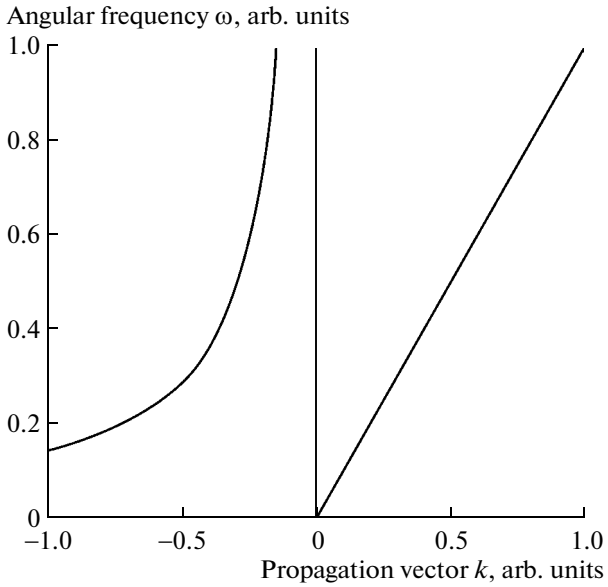

Fig. 2. Dispersion characteristics: the dependence of angular frequency ω on propagation vector k. The dispersion curves at $k > 0$ and $k < 0$ correspond, respectively, to the right-handed ($v_{ph} > 0$, $v_{gr} > 0$) and left-handed ($v_{ph} < 0$, $v_{gr} > 0$) transmission lines.

because natural transmission lines with such parameters are absent. In this case, the inverse inductance per unit length is given by

$$\left(\frac{1}{L}\right)_1 = \frac{1}{l}\frac{1}{L_0}, \quad \left(\frac{1}{C}\right)_1 = \frac{1}{l}\frac{1}{C_0}. \tag{9}$$

Here, l is the length of a unit cell in the artificial transmission line and L_0 and C_0 are the inductance and capacitance of an element in the cell. Attempts to create a left-handed transmission line in which the inverse inductance and capacitance are due to physical factors distributed along the transmission line, rather than being produced by elements concentrated in cells, have failed so far.

The dispersion characteristics (propagation vector dependences of the angular frequency) are depicted in Fig. 2. The part of the figure on the right (positive k) shows a dispersion curve corresponding to a right-handed transmission line with a positive phase velocity and a positive group velocity. The part of the figure on the left (negative k) corresponds to a left-handed transmission line with a negative phase velocity and a positive group velocity. In both cases, the phase and group velocities are given by formulas (6) and (7).

2. TWO-DIMENSIONAL AND THREE-DIMENSIONAL METAMATERIAL STRUCTURES

Left-handed materials (LHMs) were engineered and demonstrated more than 30 years after Veselago had published its work. These LHMs were artificial effectively homogeneous structures, rather than being natural substances, as Veselago expected. The structures were demonstrated by Smith with coworkers from the University of California, San Diego [13]. This achievement was based on works by Pendry et al. [14–16], from Imperial College London. They suggested a plasmon-type structure with a negative permittivity at microwave frequencies. The structure represents an array of thin metal wires.

An electric field applied parallel to the axes of the wires generates a current in them, which produces equivalent electric dipole moments. When averaged, these dipole moments reveal the structure's permittivity with a plasmon-type frequency dependence (Fig. 3a),

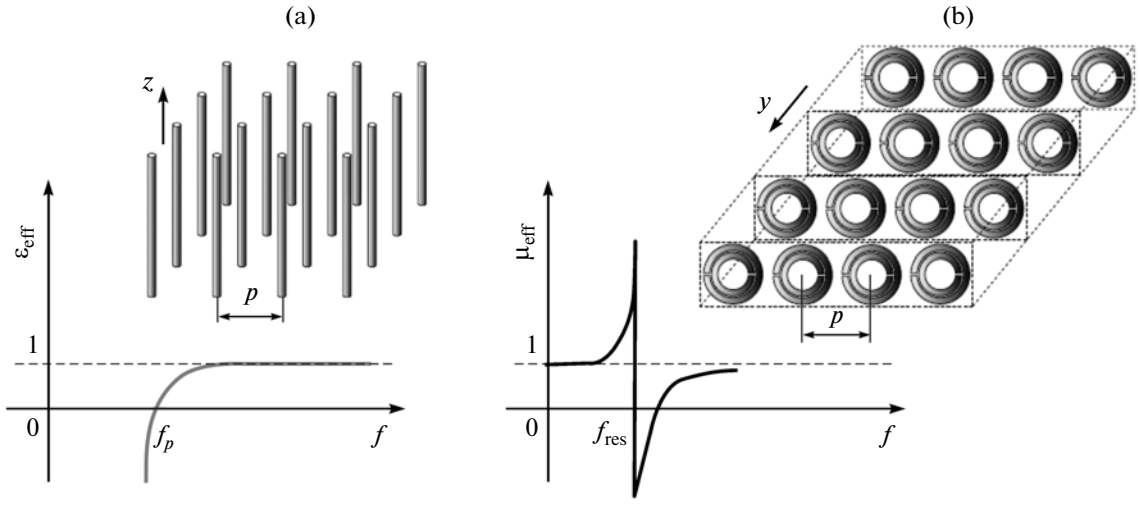

Fig. 3. (a) Array of thin metal wires. An electric field parallel to the wires excites electric dipole moments in them. (b) SRRs. At frequencies above the resonance frequency, the effective permeability of this structure is negative.

Fig. 4. Combination of structures with a negative permittivity and a negative permeability (experimental implementation).

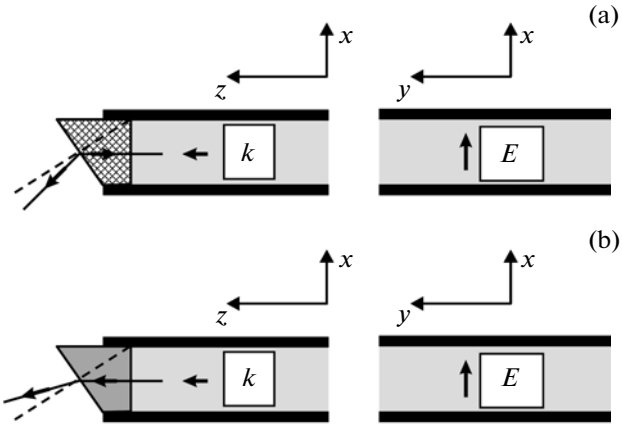

Fig. 5. Design of the experiment in which it was proved that the Snell law shows itself differently when a wave is refracted at (a) free space–metamaterial and (b) free space–normal material interfaces.

$$\varepsilon_r(\omega) = 1 - \frac{\omega_{pe}^2}{\omega^2 + i\omega\zeta}, \qquad (10)$$

where ω_{pe} is the electron plasma frequency, ζ is the damping parameter, and

$$\omega_{pe} = \sqrt{\frac{2\pi c^2}{p^2 \ln\left(\frac{p}{a}\right)}}, \quad \zeta = \frac{2\omega_{pe}^2 \varepsilon_0}{\pi\sigma}\left(\frac{p}{a}\right)^2. \qquad (11)$$

Here, p is the interwire spacing, a is the radius of the wire, c is the velocity of light, and σ is the conductivity of the wire. Interwire spacing p is much smaller than λ_g ($p \ll \lambda_g$), where λ_g is the length of the wave propagating in the structure. Thus, the structure can be considered as electrodynamically homogeneous.

A structure made up of split-ring resonators (SRRs) exhibits a resonance (Fig. 3b), the effective permeability being negative at above-resonance frequencies,

$$\mu_r(\omega) = 1 - \frac{F\omega^2}{\omega^2 - \omega_{0m}^2 + i\omega\zeta}. \qquad (12)$$

Here,

$\omega_{0m} = c\sqrt{\dfrac{3p}{\pi \ln(2wa^3/\delta)}}$ is the resonance frequency of the ring resonator,

$$F = \pi(a/p)^2, \quad \zeta = (2pR_1)/a\mu_0 \qquad (13)$$

is the damping parameter, a is the inner radius of the ring, δ is the radial distance between the rings, and R_1 is the resistance per unit length of the metal conductor.

Smith with coworkers formed a combination of structures with a negative permittivity and a negative permeability (Fig. 4) suggested by Pendry et al. The combined structure had a negative refractive index [17]. Figure 5 shows the design of the experiment from which it becomes clear that the Snell law is fulfilled if the refractive index of the sample is negative. In experiments, a plane wave propagates along the z axis between the conducting surfaces. In Fig. 5, vector **E** normal to the conducting surfaces and propagation vector **k** showing the propagation direction of the wave are depicted. The wave is incident on a negative-refractivity metamaterial. At the interface between the metamaterial and free space, the wave is refracted in such a way that the incident and refracted waves are on one side of the normal to the outer surface of the sample.

The metamaterial structure of Pendry et al. and Smith et al. is anisotropic. It controls the propagation of plane waves with a propagation vector parallel to the plane over which electric and magnetic moments are periodically arranged. Subsequently, many researchers tried to prepare an isotropic structure that has a negative refractivity irrespective of how the propagation vector and symmetry axes of the structure are oriented. For example, an artificial structure was suggested [18] in which two sublattices of high-permittivity particles are embedded in a low-permittivity matrix. The arrangement of the particles is similar to the NaCl structure and has cubic symmetry. The permittivity and permeability tensors of the resulting structure are isotropic. Particles from different sublattices differ in size, and various modes of Mie resonances [19–22] are excited in the sublattices. The frequency is used at which resonance oscillations of mode H_{111} and those of mode E_{111} arise simultaneously in particles of different size. The resonances of modes H_{111} and E_{111} give rise, respectively, to electric and magnetic dipole moments (Fig. 6). Averaging the dipole moments over cells containing the respective spherical particles makes a contribution to the permittivity and permeability of the medium [19]. At above-resonance frequencies, this contribution becomes negative, so that the permittivity and permeability of the medium

become negative simultaneously and, as a result, the refractive index also becomes negative. Note that the suggested structure consists of only dielectric components. Spherical particles with permittivity $\varepsilon_r > 200$ are prepared from ferroelectrics. The resonance frequencies of spherical particles 50–500 μm in diameter lie in the interval 5–50 GHz.

Numerical calculation based on full-wave analysis showed that the refractive index of a medium containing two sublattices of dielectric spheres, in which the resonance oscillations of modes H_{111} and E_{111} are excited, is really negative [20]. It was also shown that, if the sublattices of dielectric resonant particles exhibit cubic symmetry, the tensors of the averaged permittivity and averaged permeability are isotropic [19–22]. Along with studies of the metamaterial properties using two sublattices of noninteracting dielectric resonators, chains and arrays of coupled (interacting) dielectric resonators were simulated [23–25]. Coupling between resonators increases the contribution of the electric dipole moment to the averaged permittivity of the structure. Along with spherical inclusions, cubic dielectric inclusions were also tested [26, 27].

Isotropic metamaterials with variously shaped resonant dielectric inclusions were studied by different teams of researchers. These studies were initiated in [28], where a hypothetical regular structure with magnetodielectric spherical inclusions having the permittivity and permeability of the same order of magnitude was suggested. Subsequently, a great number of pure dielectric structures containing variously shaped resonators were tested. For example, in [29] an electrodynamic analysis was carried out of media representing (i) an array of dielectric spherical particles equal in diameter and differing in permittivity and (ii) a set of dielectric disk-shaped particles equal in diameter and differing in permittivity. In the latter case, the disks were 3D structures made up of elements with two negative electrodynamic parameters (ε, μ). The arrays of the above spherical and disk-shaped resonators exhibit the properties of metamaterials with a negative permittivity and permeability near Mie resonances of the same (magnetic) type provided that the permittivities of the resonators were properly chosen.

An array of cylindrical resonators inserted in between parallel conducting planes was theoretically and experimentally investigated in [30, 31]. The properties of these structures with the two negative parameters were determined by resonances in the cylinders. Magnetic dipoles arising in the cylinders make the medium μ-negative, coupling between neighboring cylinders playing a special role [31]. An ε-negative medium forms when an electromagnetic wave propagates in a waveguide at a below-critical frequency [30]. A waveguide with a TE_n field is used. It is composed of parallel conducting planes with vector E being normal to the conducting planes.

Isotropic metamaterials with resonant dielectric inclusions were also studied experimentally in [32–34]. Resonance ε-negative properties were observed in a 3D array of dielectric cubes [32] and in a 2D array of dielectric cubes [33]. A 3D medium with the two negative parameters was implemented by regularly placing spherical dielectric particles in the cells of a framework made up of metallic conductors with cubic symmetry [34]. The wire framework provided an environment produced by evanescent modes with a negative effective permittivity combined with a negative effective permeability of magnetic dipoles arising in resonant dielectric particles.

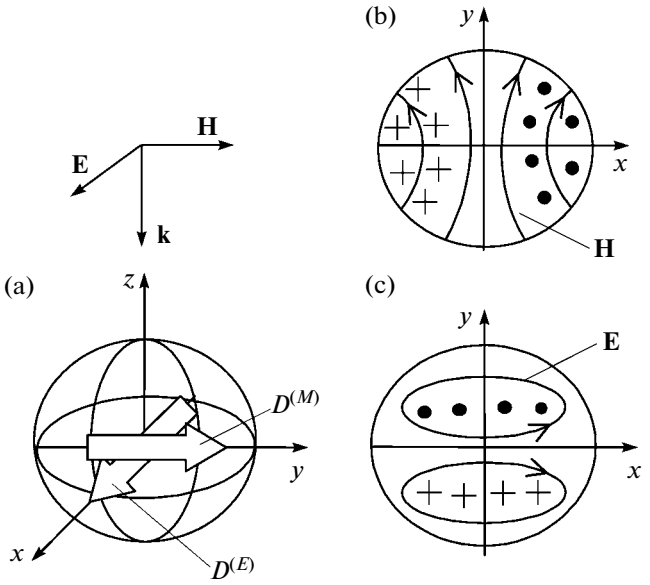

Fig. 6. (a) Electrical, $D^{(E)}$, and magnetic, $D^{(M)}$, dipole moments and oscillation modes (b) H_{111} and (c) E_{111} in spherical particles.

The above results count in favor of the idea that isotropic metamaterials can be made using dielectric resonant inclusions. The 3D medium with the two negative parameters can be refined further by correcting the symmetry of a cell in a structure consisting of two spherical particles. This will increase the contribution of the electrical resonant dipole to the effective permittivity. For example, one can improve the packing density by using the body-centered cubic structure with the interparticle spacing being the same [26].

Along with isotropic metamaterials based on symmetric dielectric resonant inclusions, it was suggested to develop isotropic materials on nonresonant cubic particles with symmetrized SRRs or Ω particles on their faces [35–37]. The examples of such isotropic metamaterials employing arrays of cubic particles with plane metallic particles on their faces are given in Fig. 7.

Thus, there exists a variety of approaches to engineering metamaterials with a negative permittivity and permeability.

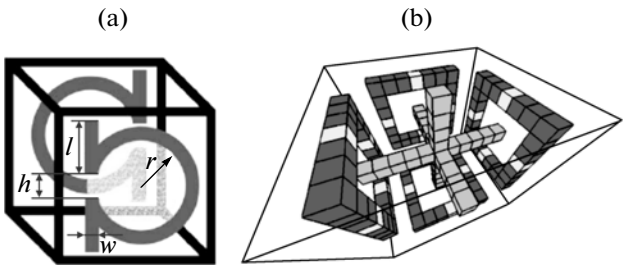

Fig. 7. Unit cubic cells with (a) Ω particles and (b) symmetrized SRRs in combination with feedthroughs applied on their faces.

3. ARTIFICIAL TRANSMISSION LINES AS ONE-DIMENSIONAL METAMATERIALS

Let us first introduce some definitions in terms of which artificial transmission lines offering the properties of metamaterials will be discussed.

Transmission lines can be subdivided into transmission lines with positive phase and group velocities or positive-dispersion transmission lines (PDTLs) and transmission lines with a negative phase velocity and a positive group velocity or negative-dispersion transmission lines (NDTLs).

Applying PDTLs and NDTLs allows designing microwave devices with extended functionality and/or radically new properties to be used in advanced telecommunication systems. PDTL- and NDTL-based microwave equipment was described in monographs [11, 12], Metamaterials Handbook [8], and articles [38, 39].

3.1. Equivalent Representation of a Transmission Line as a Lumped Reactive T or Π Circuit

A transmission line can be represented as a set of series-connected unit cells. PDTL- and NDTL-based microwave devices should be synthesized so that the parameters of unit cells can be found from given values of the characteristic impedance and electrical length of the transmission line. The main stage of synthesis is the equivalent representation of the transmission line as a lumped T or Π circuit [40, 41]. The table lists the equivalent parameters of the transmission line represented as a T or Π circuit consisting of reactive components.

Figure 8 shows the design of a unit cell of a T circuit made up of lumped parallel-plate capacitors and a lumped inductance network. All cells shown in the table can be designed in the same way.

Theoretically, one can determine the values of "negative" capacitive and inductive components of the equivalent circuit. Of course, negative reactive components can physically be implemented in exceptional cases: near the resonance frequency or by synthesizing active non-Foster circuits. Sometimes, however, when synthesizing devices based on a combination of PDTLs and NDTLs, one can use a negative inductance or capacitance if it is parallel- or series-

Equivalent parameters of a section of a transmission line in the form of a T or Π circuit

Electrical length (type) of line	Type of circuit	Electrical circuits	Reactive parameters of T or Π circuit
$0° < \theta \le 90°$ (PDTL)	T circuit	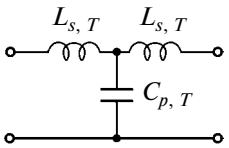	$L_{s,T} = \frac{Z_0}{\omega_0}\tan\left\lvert\frac{\theta}{2}\right\rvert$ $C_{p,T} = \frac{1}{\omega_0 Z_0}\sin\lvert\theta\rvert$
	Π circuit	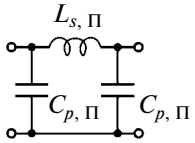	$L_{s,\Pi} = \frac{Z_0}{\omega_0}\sin\lvert\theta\rvert$ $C_{p,\Pi} = \frac{1}{\omega_0 Z_0}\tan\left\lvert\frac{\theta}{2}\right\rvert$
$-90° < \theta \le 0°$ (NDTL)	T circuit	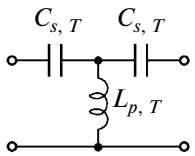	$C_{s,T} = \frac{1}{\omega_0 Z_0}\cot\left\lvert\frac{\theta}{2}\right\rvert$ $L_{p,T} = \frac{Z_0}{\omega_0}\frac{1}{\sin\lvert\theta\rvert}$
	Π circuit	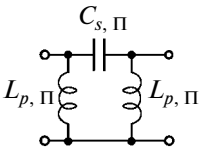	$C_{s,\Pi} = \frac{1}{\omega_0 Z_0 \sin\lvert\theta\rvert}$ $L_{p,\Pi} = \frac{Z_0}{\omega_0}\cot\left\lvert\frac{\theta}{2}\right\rvert$

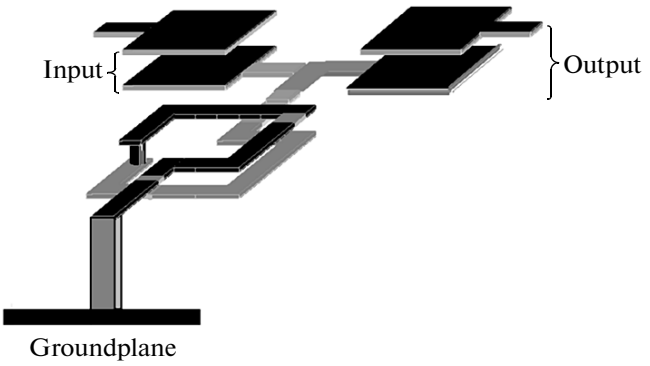

Fig. 8. Layout of the *T* circuit consisting of lumped parallel-plate capacitors and a lumped two-turn inductance.

connected to a real (positive) reactive component. In this case, the total values of the reactive components are positive. If the electrical length of the transmission line exceeds $\pi/2$, it can be implemented as a cascade connection of unit cells (see the table).

3.2. Miniaturization of a Hybrid Ring Using PDTLs and NDTLs

Figure 9a shows a microstrip hybrid ring on an dielectric substrate. The hybrid ring is, in essence, an inphase–antiphase directional coupler. The scattering matrix of a 3-dB hybrid ring has the form

$$S = \frac{-i}{\sqrt{2}}\begin{bmatrix} 0 & 1 & 1 & 0 \\ 1 & 0 & 0 & -1 \\ 1 & 0 & 0 & 1 \\ 0 & -1 & 1 & 0 \end{bmatrix}. \qquad (14)$$

The distance between neighboring inputs of the hybrid ring sets a phase shift of the wave traveling over the ring, which is equal either to $-90°$ or to $-270°$. Geometrically, the distance between neighboring inputs equals, respectively, either $\lambda/4$ or $3\lambda/4$, so that the total length of the ring is 1.5λ (λ is the wavelength in the transmission line). Let us replace $\lambda/4$- or $3\lambda/4$-long segments of long lines by sections made up of inductive and capacitive components. The $\lambda/4$-long segments are replaced by PDTLs with an electrical length of 90°, and the $3\lambda/4$ -long segment is replaced by an NDTL with a negative electrical length of $-90°$. Note that the phase shift in the 270° long line and that in the $-90°$ long line are identical. Figure 9b shows three sections formed by PDTLs and one section formed by an NDTL. Taking into account that $-i\omega C = 1/(i\omega L)$ at the center frequency, that is, that the conductivities of parallel-connected reactive components at inputs *2* and *4* are zero, we arrive at the simplified circuit of the hybrid ring depicted in Fig. 9c.

The possibility of implementing this equivalent circuit in the form of a lumped integrated circuit was studied with structures fabricated using the conventional thick-film multilayer technology [42–45] and multilayer ceramics technology [46–49]. In the latter case, the low-temperature co-fired ceramic (LTCC) method was applied. Both microstrip and coplanar strip lines were tested.

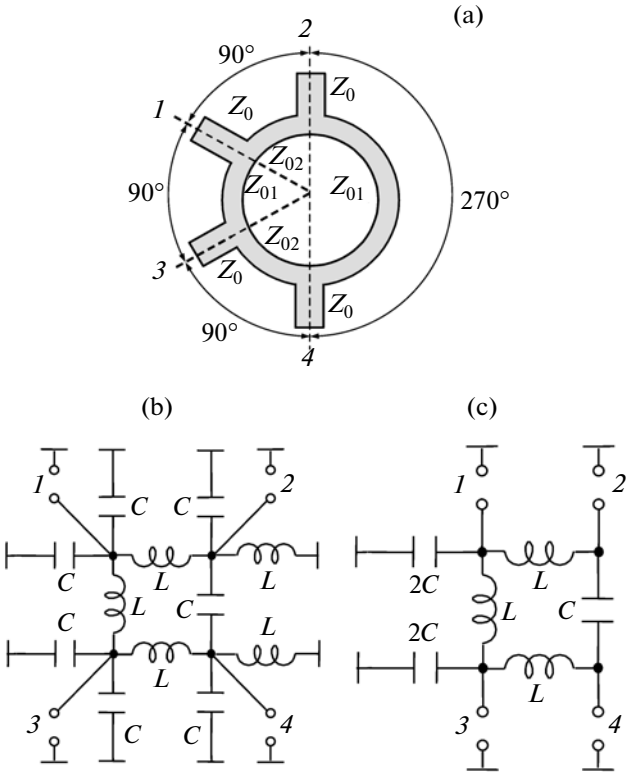

Fig. 9. Versions of the inphase–antiphase directional coupler (hybrid ring): (a) hybrid ring built around microstrip lines on an dielectric substrate, (b) hybrid ring composed of three PDTL sections and one NDTL section and (c) simplified circuit of the hybrid ring.

Figure 10a shows the layout of a multilayer hybrid ring chip (coplanar version) [49, 50]. The chip consists of eight 95-μm-thick LTCC (DuPont Green Tape 951) layers with parallel-plate capacitors and two-turn stacked inductors. Conducting layers were made of DuPont 6145 silver-based paste providing dc sheet resistance $R_{dc} = 6$ mΩ/□. After firing, the metallization thickness was 9–11 μm. The overall dimensions of the multilayer chip were $7.50 \times 7.50 \times 0.76$ mm. The linear sizes of the chip were no greater than 1/8 of the wavelength at the center frequency in the line, and the surface area of the hybrid ring was at least eight times smaller than that of the distributed-component ring (Fig. 9) made on the same substrate. Figure 10b shows the X-ray pattern of the inner layers of the chip. Its experimental characteristics and the results of electrodynamic simulation are presented in Fig. 11. In the frequency band 2.2–2.7 GHz (20%), the power division nonuniformity is no larger than ±1 dB, the input reflection coefficient and isolation ratio are no worse than −20 dB, and insertion losses are no higher than

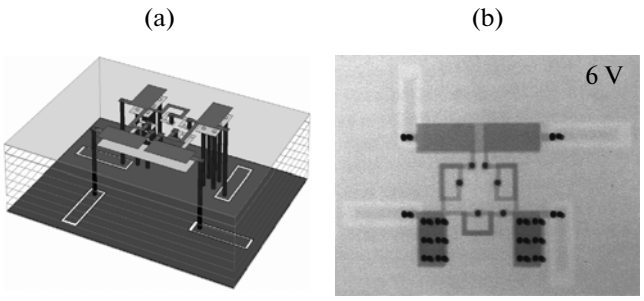

Fig. 10. (a) Multilayer chip of the hybrid ring shown in Fig. 9c (coplanar design) and (b) X-ray pattern of the chip's inner layers.

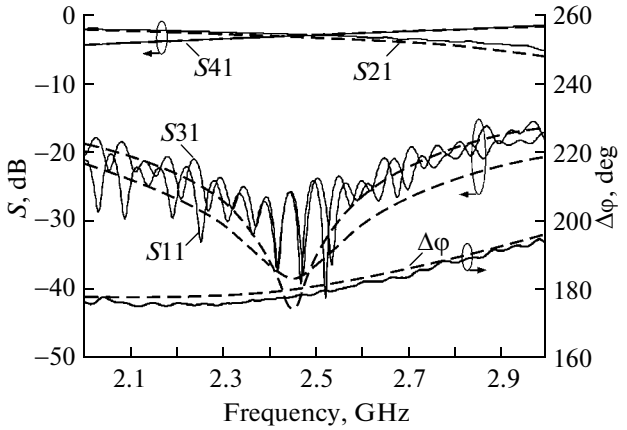

Fig. 11. Results of electrodynamic simulation (dashed lines) and experimental study of the small-size hybrid ring characteristics (solid lines).

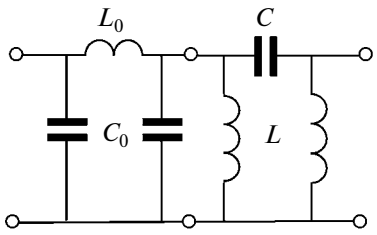

Fig. 12. Electrical circuit of the resonator made up of positive-dispersion and negative-dispersion cells.

0.2 dB. The phase difference between the signals in the antiphase mode falls into the interval 179°–187°.

The directional coupler can be miniaturized further by refining the fabrication technology. Since the electrodes of the capacitor occupy a major part of the substrate, their decrease is expected to considerably influence the overall dimensions of the chip. The surface area of the capacitors can be effectively shrunk by applying high-permittivity dielectric pastes [47]. In addition, using the approach described above (replacement of distributed-component lines by PDTLs and NDTLs) and the LTCC method, miniature directional branch couplers and a Wilkinson three-port divider combiner [51, 52] can be implemented.

3.3. Resonator Formed by PDTL and NDTL Cells

In the general case, the resonator is an oscillatory system in which the oscillation energy accumulates when the eigenfrequency of oscillations in the resonator coincides with the frequency of the exciting force. Under such conditions, the oscillation amplitude of the resonator becomes maximal. The maximal amplitude is limited by losses in the resonator. The frequency at which the amplitude reaches a maximal value is called the resonance frequency. A resonator formed by sections of a transmission line or consisting of a large number of unit cells with lumped components is characterized by a discrete spectrum of resonance frequencies.

Figure 12 shows the resonator circuit consisting of a positive-dispersion cell cascade-connected to a negative-dispersion cell. A wave passing through the positive-dispersion cell acquires a phase delay, while after passing the negative-dispersion cell, it acquires a phase advance. As a result, the phase of the wave having passed through both cells with the same absolute electrical length remains unchanged. Such a resonance with a zero phase shift is called the zeroth-order resonance.

Figure 13 shows circuit analysis data for the parameters of a zeroth-order resonator. The values of the components were $L = L_0 = 7$ nH and $C = C_0 = 0.45$ pF; accordingly, the resonance frequencies in both cells were $f = f_0 = 8.967$ GHz. In Fig. 13a, the frequency dependences of the transmission and the reflection coefficient of the resonator are plotted. The transmission coefficient is seen to be maximal at the resonance frequency. Accordingly, the reflection coefficient is minimal at the same frequency. Figure 13b shows the phase shift of the wave having passed through both cells. At the resonance frequency, it equals zero. This means that the zeroth-order resonance is observed in this case.

Of interest is the group delay of a wave packet propagating through the resonator,

$$\tau_{gr} = \frac{d\varphi}{d\omega}. \quad (15)$$

The frequency dependence of the group delay is presented in Fig. 13c. It reaches a maximum at the resonance frequency. This is because the energy accumulated in the resonator also reaches a maximum at the resonance frequency, and the energy accumulation certainly takes some time.

Consider cascade-connected pairs of cells of PDTLs and NDTLs. A set of PDTL/NDTL cells has a discrete spectrum of resonance frequencies, at which the transfer ratio is maximal. The resonance frequencies

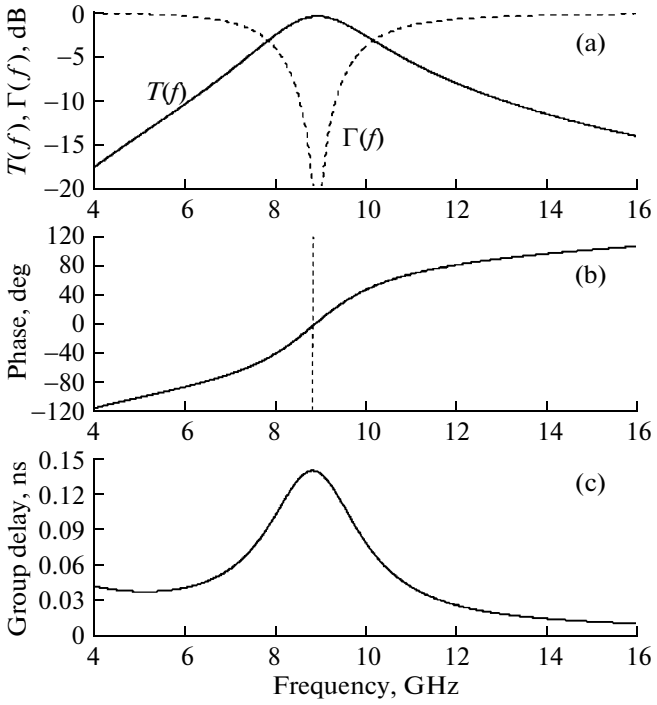

Fig. 13. Parameters of the zeroth-order resonator: (a) transmission ratio and reflection coefficient, (b) phase incursion, and (c) group delay.

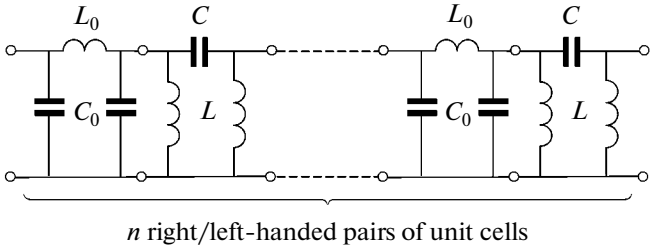

Fig. 14. *n* cascade-connected pairs of PDTL/NDTL cells.

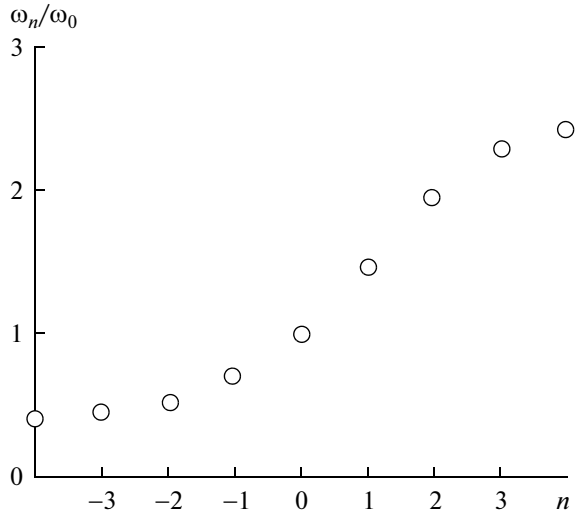

Fig. 15. Normalized resonance frequencies of *n* cascade-connected pairs of PDTL/NDTL unit cells.

can be found by solving the respective dispersion equations derived from the Bloch–Floquet theory [11, 53]. For a pair of PDTL/NDTL cells, one can find two resonance frequencies for series (ω_{01}) and parallel (ω_{02}) resonances,

$$\omega_{01} = 1/\sqrt{L_0C}, \quad \omega_{02} = 1/\sqrt{LC_0}. \qquad (16)$$

In the simplest case, $\omega_{01} = \omega_{02} = \omega_0$. For one of the cells, ω_0 is the resonance frequency. For $N + 1$ cascade-connected pairs of cells, the Bloch–Floquet theory yields the following dispersion relation:

$$2 - \frac{1}{2}\left(\frac{\omega_0^2}{\omega_n^2} + \frac{\omega_n^2}{\omega_0^2}\right) = \cos\left(\frac{n\pi}{N}\right), \qquad (17)$$

where n is the number of resonance.

As one example, consider five pairs of PDTL/NDTL cells. In this case, $N = 4$ and the number of resonance lies in the interval $-4 < n < 4$ (including $n = 0$); that is, we have nine resonances. Figure 15 demonstrates the result of the solution of Eq. (17): the normalized resonance frequencies versus the number of resonance. This solution was obtained for the case when the resonator consisting of five pairs of PDTL/NDTL cells is terminated by an infinitesimal external resistance. Then, if the Q factors of components in the cells are finite, the transmission coefficient tends to zero. Actually, the transmission coefficient is other than zero, since so is the external load. The frequency dependences of the transmission and the reflection coefficients of the resonator calculated for the given structure with five pairs of unit cells are shown in Fig. 16a. At frequencies above the zeroth resonance frequency, $f_n > f_0$ at $n = 1$–4; at frequencies below the zeroth resonance frequency, $f_n < f_0$ at $n = -1$ to -4. The total number of resonances is $2N - 1$, where N is the number of pairs of PDTL/NDTL cells. These resonances are usually referred to as nth-order resonances for $n > 0$ and $-n$th-order resonances for $n < 0$. Note that for even resonances, the phase shift of a wave having passed through the resonator is 0° or ±360°. Accordingly, for odd resonances, the phase shift equals ±180° or ±540°. The phase shifts are shown in Fig. 16b, and Fig. 16c plots the group delay of the signal in the resonator versus the frequency. The same phase shifts as in Fig. 16b are also observed when a wave propagates in a resonator based on a standard transmission line. The resonance current distributions over a long line section accommodating one or three current half-waves and zero, two, or four current half-waves are depicted in Fig. 17. In the former case, the phase shift of the wave having passed through the resonator is 180° or 540°; in the latter, 0°, 360°, or 720°.

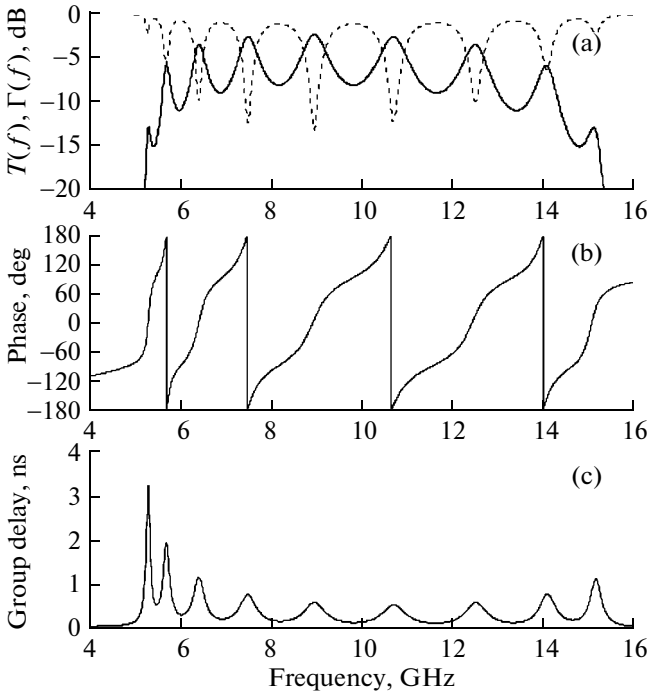

Fig. 16. Parameters of the resonator made in the form of n cascade-connected PDTL/NDTL unit cells: (a) transmission and reflection coefficients, (b) phase incursion, and (c) group delay.

3.4. Dual-Frequency Resonator and a Dual-Band Filter Based on PDTL/NDTL Unit Cells

Let us see how to synthesize, implement, and test microwave devices based on PDTL and NDTL cells. Of interest are, in particular, multi-mode resonators with an arbitrary set of resonance frequencies. Figure 18a shows the circuit of a resonator made up of a negative-dispersion transmission line (at the center) and two positive-dispersion transmission lines. Such a resonator can be implemented by cascade connection of PDTL and NDTL unit cells, as shown in Fig. 18b. The NDTL cell at the center has the form of a T circuit, and the PDTLs are replaced by short sections of a natural transmission line that are series-connected to a positive-dispersion cell in the form of a Π circuit. The electrical length of the negative-dispersion T cell is $2\theta_L < 0$, that of either section of the natural transmission line is $\theta'_R > 0$, and the electrical length of the positive-dispersion Π cell is $\theta_R > 0$. The wave impedance of the negative-dispersion cell is Z_L, and the wave impedance of the section of the natural transmission line and the positive-dispersion cell is Z_R. The electrical length of either section of the line depends on the frequency,

$$\theta_L(\omega) = \theta_{0L}\frac{\omega_0}{\omega}, \quad \theta_R(\omega) = \theta_{0R}\frac{\omega}{\omega_0}. \qquad (18)$$

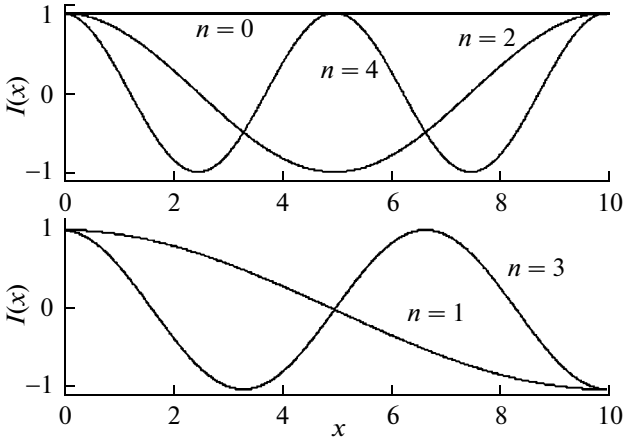

Fig. 17. Current resonance distribution over a section of a long line for the even (upper panel) and odd (lower panel) number of half-waves.

Here, θ_{0L} and θ_{0R} are the electrical lengths of the PDTL and NDTL cells, respectively, at frequency ω_0. The electrical length of the negative-dispersion cell decreases with increasing frequency, whereas that of the positive-dispersion cell grows with frequency, the effective length of the whole resonance circuit increasing by a half-wavelength when passing to the next higher order resonance.

Let us now find resonance conditions for two modes corresponding to the first ($n = 1$) and second ($n = 2$) resonances in the resonator depicted in Fig. 18b. Assuming that the capacitance of coupling between the resonator and external transmission lines is small, we will consider the resonator as a circuit open-ended on both sides. If the structure is symmetric and $n = 1$, we have a short-circuit plane at the center. At $n = 1$ and $\omega = \omega_0$, the impedance at the joints of the transmission lines with different wave impedances is

$$Z_1 = iZ_L\tan(\theta_{0L}) \qquad (19)$$

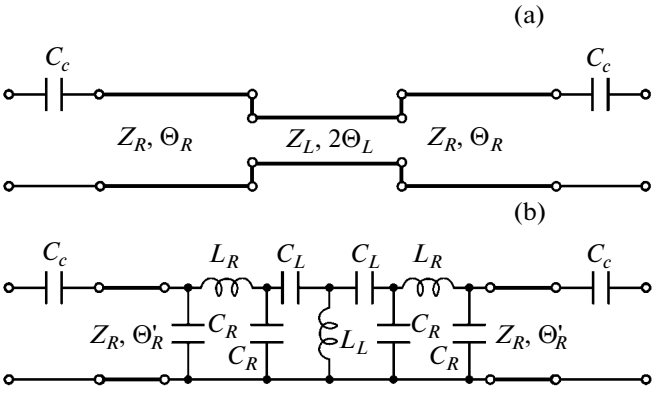

Fig. 18. Resonator made up (a) of transmission line sections and (b) by cascade connection of unit cells with different dispersion laws.

on the side of the negative-dispersion line and

$$Z_2 = -iZ_R\cot(\theta_{0R}) \quad (20)$$

on the side of the positive-dispersion line. The resonance condition is $Z_1 = Z_2$. Eventually, we arrive at a dispersion relation for the frequency of the resonance frequency of the resonator's fundamental mode ($n = 1$),

$$Z_L\tan(\theta_{0L} = -Z_R\cot(\theta_{0R}). \quad (21)$$

With regard to dispersion relations (18), we obtain a dispersion relation for the second resonance ($n = 2$) with frequency ω_1,

$$Z_L\cot\left(\theta_{0L}\frac{\omega_0}{\omega_1}\right) = Z_R\cot\left(\theta_{0R}\frac{\omega_1}{\omega_0}\right). \quad (22)$$

Figure 19 plots the resonator's transmission coefficient against the frequency for different wave impedance ratios Z_R/Z_L. A remarkable feature of such a resonator is that the frequencies of the first and second resonances are not multiples even at $Z_R = Z_L$. This is because the electrical lengths of the positive-dispersion and negative-dispersion cells variously depend on the frequency.

The layout of the resonator with the equivalent circuit shown in Fig. 18b is presented in Fig. 20. It is made up of inductive and capacitive components obtained by the multilayer LTCC technology [51, 54] using DuPont Green Tape 951 materials. The resonator has eight 95-μm-thick layers with permittivity $\varepsilon_r = 7.8$. The chip dimensions are $22 \times 20 \times 0.76$ mm. Note that the first resonance frequency $f_0 = 2$ GHz (the wavelength is $\lambda = 150$ mm) corresponds to the resonance with $n = 1$. The linear size of the chip is close to $\lambda/8$. The nearest resonance ($n = 2$) takes place at 3 GHz. The experimental resonator has coupling capacitance $C_c = 0.3$ pF and the electrical length of the natural transmission line $\theta'_R = 24°$. The parameters of the PDTL and NDTL were $C_R = 1.2$ pF, $L_R = 3.9$ nH, $C_L = 4.0$ pF, and $L_L = 9.8$ nH. The photo of the resonator on a test bench is shown in Fig. 21, and the calculated and measured frequency dependences of the scattering matrix parameters of the resonator [54, 55] are plotted in Fig. 22. The considerable distance between the frequencies of parasitic resonances is worth noting. The parasitic transmission bands are observed at 9–10 GHz. This is explained by the different frequency dispersions of positive-dispersion and negative-dispersion cells.

A second-order filter was synthesized using two resonators. It has two frequency bands at nonmultiple frequencies. The layout of the dual-band filter based on resonators like that shown in Fig. 20 is presented in Fig. 23a. It was fabricated using DuPont Green Tape 951 LTCC materials. The filter has eight 95-μm-thick layers, and the chip of the filter measures $24 \times 14 \times 0.76$ mm. The photo of the filter on the test bench is shown in Fig. 23b. Two transmission bands of the filter are due to using dual-frequency resonators. Figure 24 shows the calculated and measured parameters of the dual-frequency second-order filter [54–57]. Insertion losses equal 2 dB at 2 GHz and 4 dB at 3 GHz. It is seen that parasitic transmission bands are suppressed up to 12 GHz.

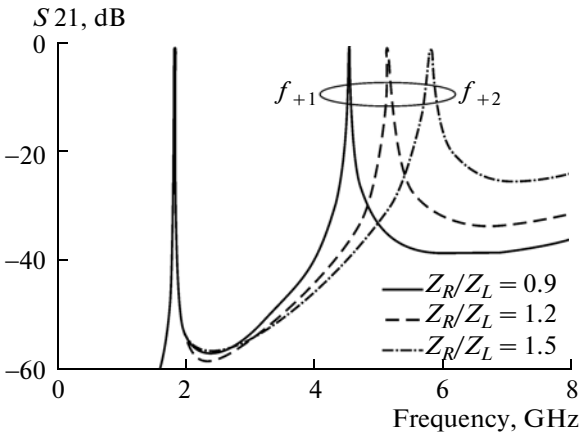

Fig. 19. Frequency dependence of the transmission coefficient of the resonator shown in Fig. 18 for different wave impedance ratio Z_R/Z_L.

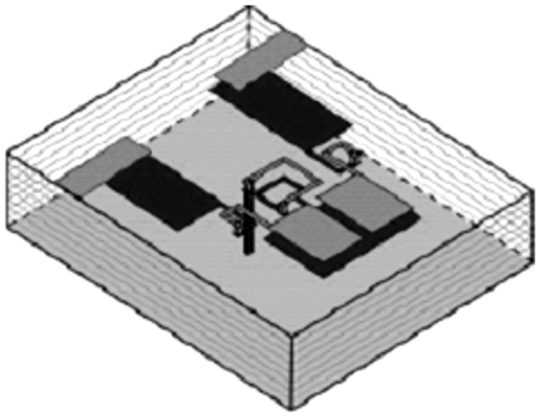

Fig. 20. Chip of the resonator with the equivalent circuit shown in Fig. 18.

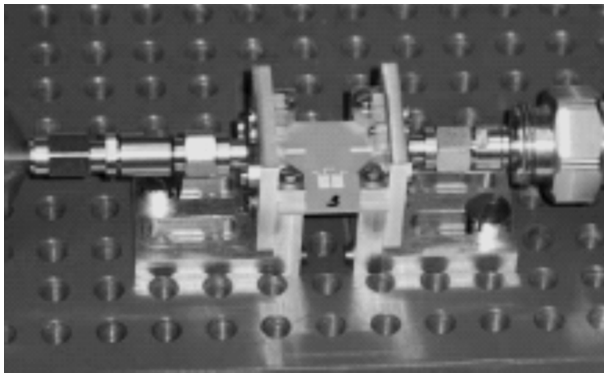

Fig. 21. Photo of the resonator (shown in Fig. 20) on the test bench.

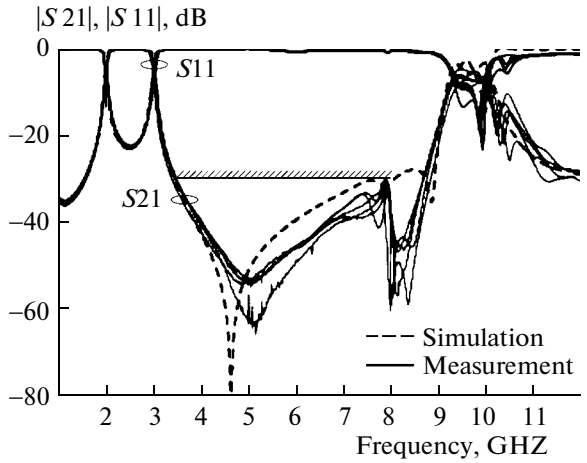

Fig. 22. Calculated and measured parameters of the scattering matrix of the resonator depicted in Fig. 20.

3.5. Phase Shifter Based on PDTLs and NDTLs

A phase shifter, a component of the microwave channel, changes the phase of a reflected or transmitted wave. The phase shifts due to an external control action (application of a voltage, current, or magnetic field). Phase shifters find wide application in phased-array antennas.

Consider a microwave 180° phase shifter based on switchable PDTL and NDTL sections in which *p–i–n* diode switches are used [58, 59]. Its circuit is shown in Fig. 25. The NDTL is made in the form of two cascade-connected *T* cells, and a distributed coplanar transmission line is used as a PDTL. The transmission lines represent two 15-μm-thick metallization layers separated by a 60-μm-thick insulating layer with permittivity $\varepsilon_r = 10.2$.

The wave impedance of both lines is 50 Ω. A control voltage is applied to the *p–i–n* diodes by lumped bias circuits (Fig. 25).

The device was fabricated by thick-film multilayer technology on a 1-mm-thick alumina substrate. Off-surface-mount *p–i–n* diodes and components of the bias circuits were used. The chip of the phase shifter measures 21.0 × 14.0 × 1.1 mm. The layout of the phase shifter built on switchable PDTL and NDTL sections and its photo are presented in Fig. 26. The NDTL uses planar capacitors with stacked plates in two conducting layers. NDTL inductances made in the lower metallization layer are connected through metallized vents to the grounded screen of the coplanar structure, which is placed in the upper metallization layer. A section of a coplanar waveguide that serves as a PDTL is also in the upper metallization layer.

Experimental phase shift-versus-frequency characteristics are shown in Fig. 27. The operating frequency band of the designed phase shifter is 2.0–3.6 GHz. In this frequency interval, the measured phase shift is 180° ± 7°; the reflection coefficient, 14 dB; and insertion loss, 0.75 dB.

In digital transmission phase shifters, a set of phase states are usually achieved. This is provided by cascade connection of single-stage phase shifters, each introducing a certain phase shift. The minimal phase shift, Δφ, is called the phase shift discrete. To obtain a set of *p* phase states spaced a phase shift step apart and providing the phase variation in the interval 0°–360°, one should cascade *m* single-stage phase shifters, which are called the sections of the transmission phase shifter. The number of sections and the number of phase states are related as

$$p = 2^m. \quad (23)$$

The phase shift provided by the *i*th section is

$$\Delta\varphi_i = 2\pi/2^i, \quad i = 1, 2, \ldots, m. \quad (24)$$

Figure 28a shows the chip layout of a three-section phase shifter using *p–i–n* diodes that is intended for 2–4 GHz [60]. As the highest order section providing a shift by 180° ± 7°, the single-section phase shifter described above is employed. Sections providing phase shifts of 90° ± 4° and 45° ± 2° are designed on the same principle but use NDTL sections based on a single unit

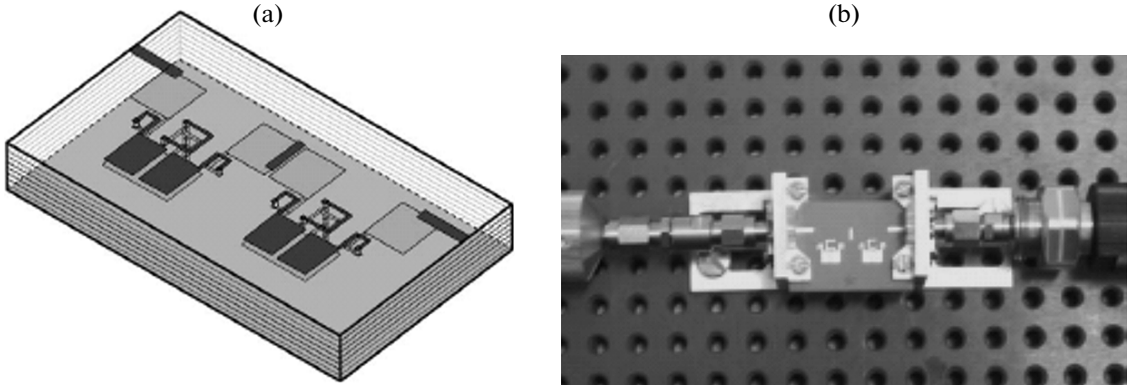

Fig. 23. Layout of the dual-band filter made up of two resonators like that depicted in Fig. 20.

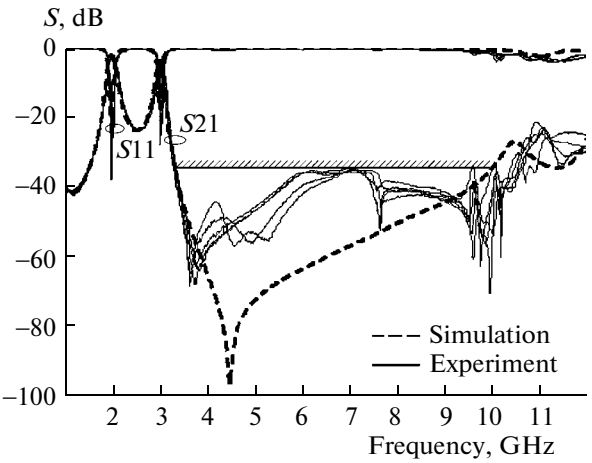

Fig. 24. Calculated and measured parameters of the dual-frequency second-order filter.

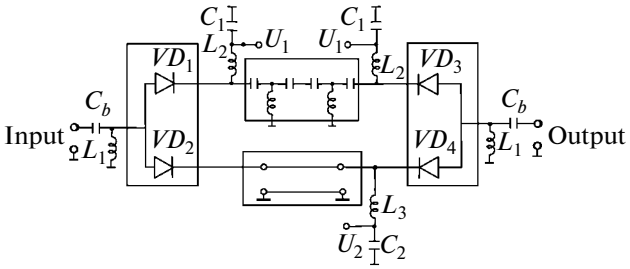

Fig. 25. Switchable-channel phase shifter. One channel is an NDTL; the second, a PDTL.

T cell. As PDTLs, coplanar waveguide sections are used in all sections. Three sections of the phase shifter are integrated into a hybrid chip, which was fabricated by the same technology as the single-stage 180° phase shifter and measures 45.0 × 18.0 × 1.1 mm.

Figures 28b and 28c demonstrate the characteristics of the three-section phase shifter for all eight states. The characteristics were obtained by electrodynamic simulation with regard to the parameters of the *p–i–n* diodes in the on and off states and the parameters of the components of the bias circuits. In the operating frequency range, the phase shifter provides an input reflection coefficient of –15 dB for any state and a phase shift error within ±8°. Insertion losses do not exceed 1 dB.

The above examples suggest that wideband digital phase shifters with a small phase shift error based on switchable PDTL and NDTL sections are feasible. The operating frequency band determined from the minimum of the phase shift error is the widest if the absolute electrical lengths of the PDTL and NDTL sections at a center frequency are the same. Phase shifters based on switchable PDTLs and NDTLs are easy to synthesize, design, and implement using the multilayer technology. Such phase shifters extend the application range of metamaterials.

4. TRANSMISSION LINES TERMINATED BY SPLIT-RING RESONATORS

Let us see how SRRs and complementary SRRs (CSRRs) terminating transmission lines influence their properties. CSRRs are made of conductive strips on the surface of an insulating substrate (Fig. 29a). CSRRs have the form of slot lines in a metal layer on the surface of a dielectric substrate (Fig. 29b). The geometries of the SRRs and CSRRs are identical. SRR- and CSRR-based transmission lines offer the properties of metamaterials. Another interesting application of SRRs and CSRRs following from their resonance nature is their use in designing filters. In addition, SRRs and CSRRs can be applied in designing impedance inverters, directional couplers, and power dividers. With a semiconductor voltage-variable capacitor inserted in the gap of the SRR, one can produce tunable filters.

4.1. Transmission Lines Terminated by SRRs and CSRRs Offering Metamaterial Properties

An original transmission line offering the properties of a metamaterial is that periodically terminated by SRRs or CSRRs. Figure 30a shows a set of SRRs connected to a coplanar line [8, 12]. The resonators are excited by a magnetic field generated in the gaps of the coplanar line. At a frequency slightly above the resonance frequency of the SRR, it exhibits the properties of an element with negative permittivity, which introduces a negative inductance per unit length into the line. The coplanar line (with wave impedance Z_0) is formed on an Arlon 250 0.49-mm-thick insulating substrate with permittivity $\varepsilon_r = 2.43$. The width of the central conductor is $w = 1.2$ mm, the outer diameter of the resonator is 5 mm, and the center distance of neighboring resonators is 3 mm. The SRRs are made by planar technology on the back (nonplated) side of the coplanar line. Figure 30b plots the frequency dependences of the calculated and measured parameters of the scattering matrix of the coplanar line terminated by four pairs of SRRs. In the frequency range where the permeability of the line is negative, a wave propagating in the line very rapidly decays.

To implement a negative-dispersion transmission line, it is necessary to provide a negative permittivity and negative permeability. To this end, additional elements that provide a negative permittivity should be introduced into the SRR-terminated line. This can be done, in particular, using inductive elements connected in parallel to the transmission line. For example, in the case of the coplanar transmission line, narrow conducting stripes can connect the central conductor of the line with its "banks." Such a configuration is depicted in Fig. 31a. In the frequency range where an effective negative permittivity and an

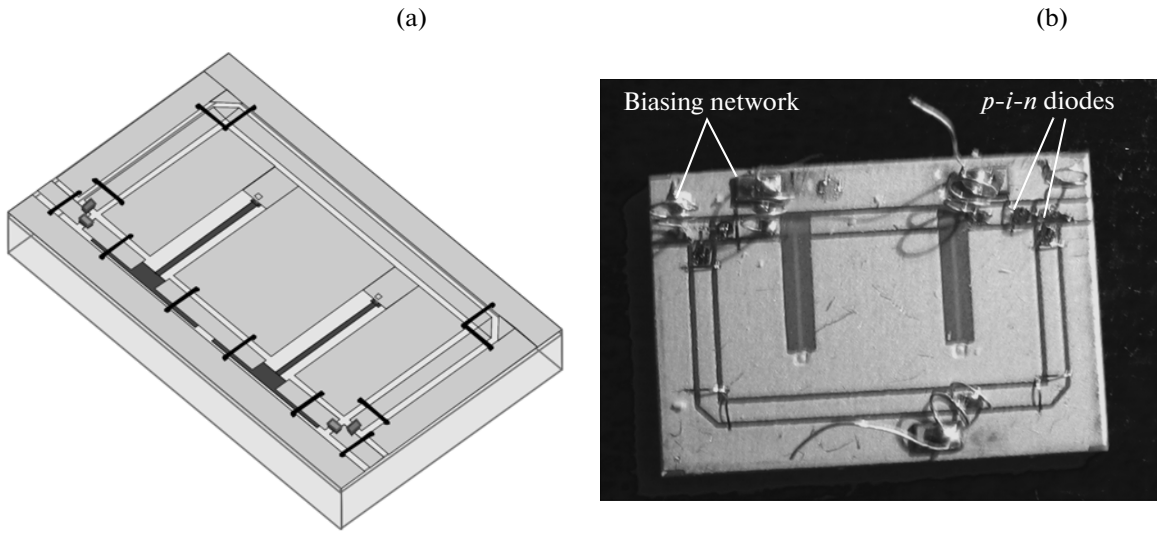

Fig. 26. (a) Layout of the phase shifter based on switchable PDTL and NDTL sections and (b) photo of this phase shifter.

effective negative permeability exist simultaneously, a wave with a negative phase velocity arises in the line. Figure 31b plots the frequency dependences of the calculated and measured parameters of the scattering matrix of the coplanar line terminated by four pairs of SRRs and four pairs of inductive bridges. In the frequency range corresponding to the metamaterial state of the line, the wave propagating in it decays negligibly, which means the propagation of a backward wave.

4.2. Band-Rejection Filters

Small-size band-rejection filters are also implemented using SRR- or CSRR-terminated transmission lines. Figure 32 shows the photo of a microstrip band-rejection filter in which the microstrip is connected to a set of CSRRs made on the back (plated) side of the substrate under the stripline. Under resonance conditions, the energy of a propagating wave is picked up by the CSRR, which causes decay in the main microstrip line. This decay becomes responsible for a stop band within the resonance curve of the CSRR (Fig. 32b). Since the Q factor of the CSRR is rather high, the stop band is narrow, so that a wide stop band is difficult to obtain. If the sizes of neighboring CSRRs differ slightly, one can separate their resonance frequencies and thereby obtain a desired wide stop band [8, 12]. Such band-rejection filters make it possible to obtain a stop band of a desired width with low losses beyond the stop band retained. Obviously, an increase in radius r will decrease the resonance frequency of SRRs or CSRRs. These miniature rejection filters are suitable for suppressing undesired transmission bands beyond the main transmission band of composite band-rejection filters.

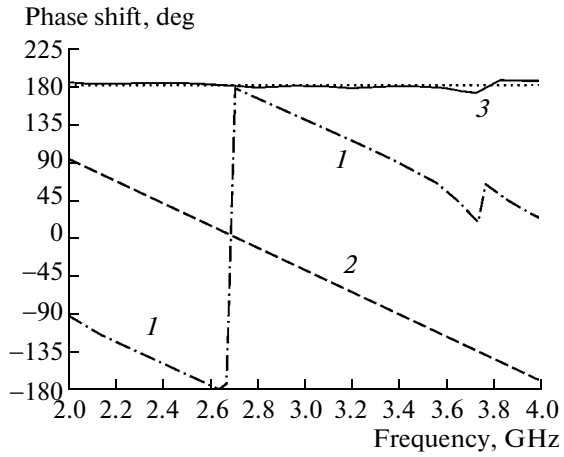

Fig. 27. Experimental frequency dependences of the phase shift over the (*1*) PDTL section and (*2*) NDTL section and (*3*) the phase difference due to channel switchover.

5. COMPOSITE TRANSMISSION LINES WITH METAMATERIAL PROPERTIES

The idea of transmission lines exhibiting the properties of metamaterials was suggested by Itoh and Kaloz in 2003 [12, 61].

Figure 33 shows a transmission line containing series-connected capacitors and parallel-connected short-circuited sections of transmission lines. The equivalent circuit of a unit cell of this transmission line is depicted in Fig. 34. The series circuit contains capacitor C_L and an inductive section of the transmission line (the inductance of the section is L_R). These reactive components form a series resonance circuit with resonance frequency ω_{se}. The short-circuited part of the transmission line is represented by a parallel circuit with capacitor C_R and inductance L_L. This circuit

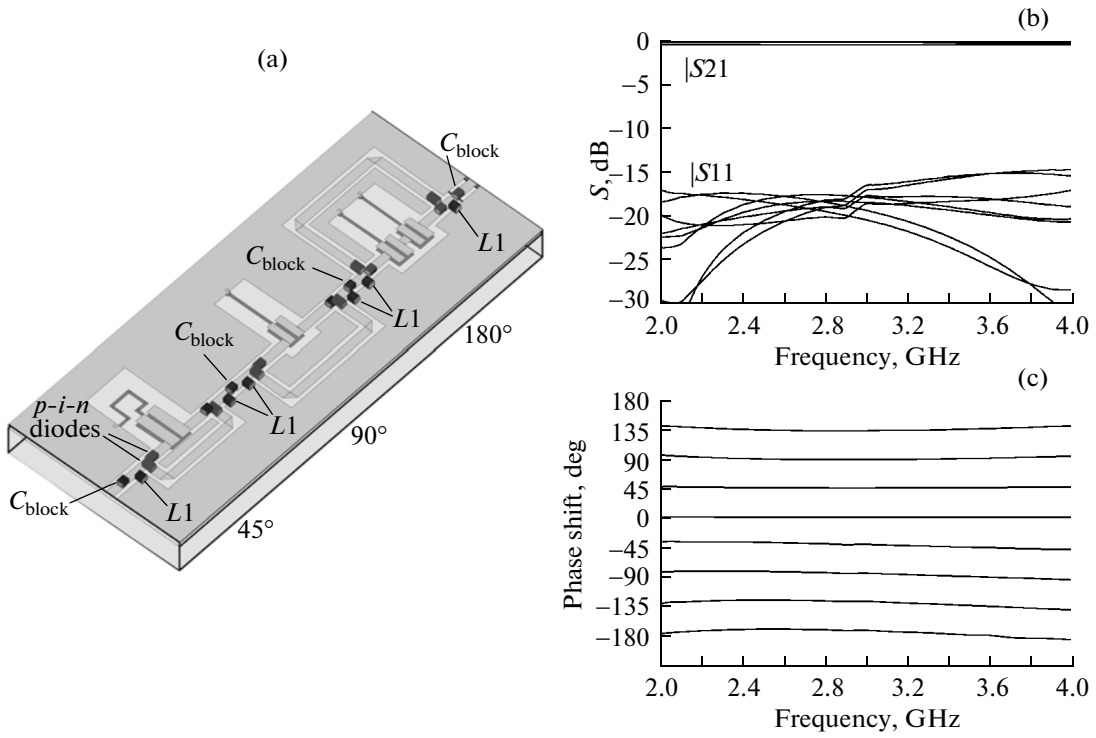

Fig. 28. Design and characteristics of the PDTL- and NDTL-based three-section switchable-channel phase shifter.

has resonance frequency ω_{sh}. At low frequencies, the properties of the transmission line are determined primarily by parameters L_L and C_L, which provide a negative phase velocity of the wave in the transmission line, that is, impart the properties of an NDTL to the line. At high frequencies, the properties of the transmission line are governed primarily by reactive components L_R and C_R, which provide a positive phase velocity of the wave in the transmission line, that is, impart the properties of a PDTL to the line (subscripts R and L refer to the right- and left-handed transmission lines, respectively).

5.1. Dispersion Properties of a Unit Cell of the Composite Transmission Line

Curves *2* and *4* in Fig. 35 are the dispersion curves of the cell presented in Fig. 34. Curves *1* and *3* correspond to ideal PDTLs and NDTLs.

At high frequencies, the absolute value of the impedance of C_L tends to zero, while that of the impedance of L_L goes to infinity; accordingly, the cell contains only series inductance L_R and parallel capacitance C_R. In this form, the cell acts as a low-pass filter with upper cutoff frequency ω_{sh}. The upper cutoff frequency is typical of PDTLs. Accordingly, at low frequencies, the cell has the properties of a high-pass filter with lower cutoff frequency ω_{se}. The lower cutoff frequency is typical of NDTLs. In general, frequencies ω_{sh} and ω_{se} differ and therefore there exists a forbidden gap between the positive-dispersion and negative-dispersion regions (Fig. 35a). However, if these frequencies are the same, the forbidden gap disappears (Fig. 35b). In this case, the cell is said to be "balanced" and the length of a wave propagating in the transmission line at frequency ω_0 goes to infinity.

Despite the "filtering nature" of the composite structure, it is never used at the edge of the Brillouin zone, since the cells of the transmission line and the line itself are discrete and so the line cannot be considered as an effectively homogeneous medium. Certainly, real dispersion curves for the regions with the PDTL and NDTL properties differ from those for ideal transmission lines with positive dispersion

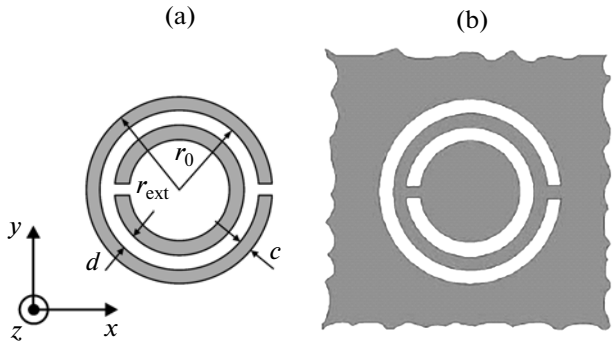

Fig. 29. (a) SRR and (b) CSRR.

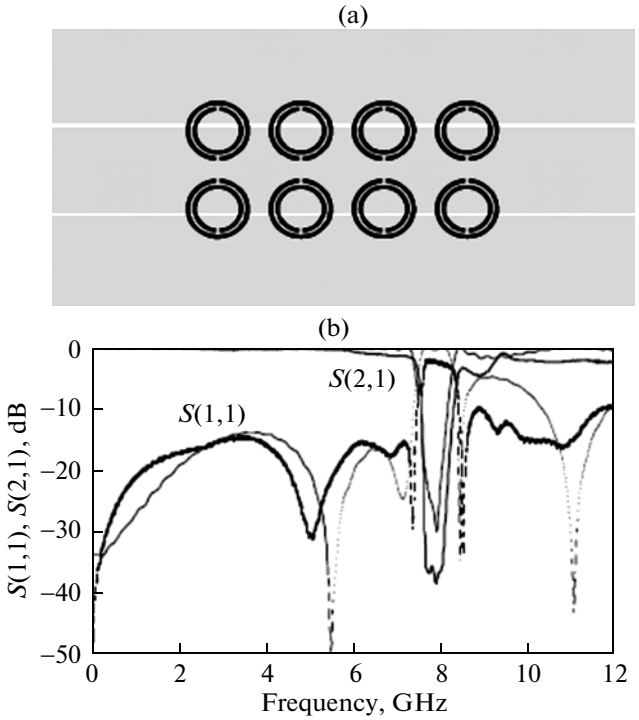

Fig. 30. (a) Coplanar transmission line coupled with a set of SRRs and (b) calculated (dashed curves) and measured (solid curves) parameters of the scattering matrix for the coplanar line terminated by four pairs of SRRs.

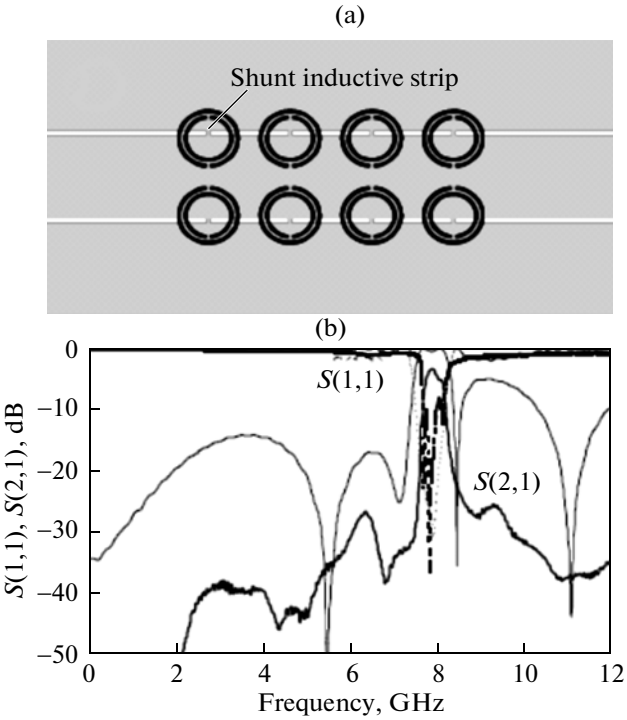

Fig. 31. (a) Coplanar line terminated by the SRR and parallel-connected narrow conducting strips in the gap serving as inductances and (b) calculated (thin curves) and measured (thick curves) parameters of the scattering matrix for the negative-dispersion coplanar line.

($L_L \longrightarrow \infty, C_L \longrightarrow \infty$) and negative ($L_R \longrightarrow 0, C_R \longrightarrow 0$) dispersion (PDTL and NDTL, respectively).

5.2. Directional Coupler Based on Composite Transmission Lines

Figure 36 shows the photo of a directional coupler consisting of cells of a composite transmission line that, in turn, is formed by series-connected capacitors and parallel-connected short-circuited sections of transmission lines [62]. The center frequency of the directional coupler is 3 GHz. The substrate material is a Rogers RT/duroid 5880 high-quality insulator with $\varepsilon_r = 2.2$ and $\tan\delta = 0.0009$. The thickness of the substrate is $h = 1.5$ mm, the width of the microstrip transmission lines is $w_c = 4.8$ mm, the spacing between the microstrip transmission lines is 0.3 mm, and the size of the cell is $d = 12.2$ mm.

The equivalent circuit of the cell is depicted in Fig. 37. Together with the components forming the cell, the equivalent circuit includes elements providing coupling between two parallel transmission lines. These are capacitor C_m for electrical coupling between the lines and mutual inductance L_m for magnetic coupling between the lines.

Figure 38 shows the calculated and measured values of the scattering matrix parameters for the directional coupler [62]. The frequency dependences of elements S_{21} and S_{31} of the scattering matrix are worthy to note. These elements characterize the transfer of the wave energy from channel no. 1 to channel no. 2 or channel no. 3. In the frequency interval 1.75–2.75 GHz, the energy in channel no. 1 almost completely passes into channel no. 2, while in the interval 3.5–4.5 GHz, the energy in channel no. 1 is almost completely transferred to channel no. 3. Such operating conditions of the coupler are illustrated by designations in Fig. 36. The above frequency dependence of the scattering matrix parameters indicates the metamaterial properties of the composite transmission lines applied in the given device. Now we turn to Fig. 35 and note that $\omega_{se} \cong 2.75$ GHz and $\omega_{sh} \cong 3.5$ GHz. The interval between ω_{se} and ω_{sh} is a forbidden gap where the energy transfer is absent. In the low-frequency range ($\omega < \omega_{se}$), propagating waves have a negative phase velocity (NDTL), while in the high-frequency range ($\omega > \omega_{sh}$), traveling waves have a positive phase velocity (PDTL). Conditions for the energy transfer from one transmission line to the other are different for NDTLs and PDTLs.

A directional coupler in which the energy of a wave almost entirely passes into one channel is usually called the 0-dB directional coupler. In the case considered above, the directional coupler serves as a duplex or a diplexer. Examples are known when a 0-dD

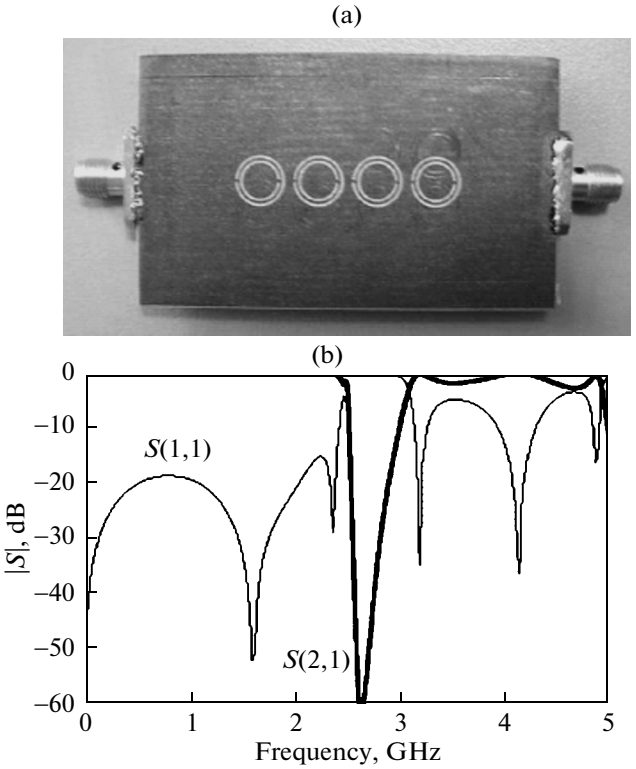

Fig. 32. (a) Photo of the stop-band filter on a microstrip line coupled with a set of CSRRs and (b) its frequency characteristic. The plated side (screen) of the microstrip line, on which the CSRRs are made, is seen in the photo.

directional coupler is used for dc isolation in microwave transistor amplifiers [63].

6. METAMATERIALS IN ANTENNA TECHNOLOGY

The components of electromagnetic circuits that offer the properties of metamaterials are finding application in the antenna technology at high frequencies (0.1–100.0 GHz). Reviews [64–66] are devoted to the application of metamaterials in antennas. In this field, metamaterials are largely used in radiators placed above a high-impedance surface and in antennas with surface wave radiation (surface-wave antennas). In addition, they can be employed to suppress interaction between elements of antenna arrays, including in multiple-input multiple-output (MIMO) devices, and to increase the gain of a horn antenna.[1]

6.1. High-Impedance Surface

Consider the properties of the interface between free space and an artificial material. Our goal is to tailor a material the surface impedance of which relative to a microwave far exceeds the wave impedance of free space, $Z_0 = 120\ \Omega$. The surface with such a high impedance is usually called "the magnetic wall." It is well known that the surface impedance of a conductor relative to a microwave equals several hundredths of Ohm. A good conductor (metal) is generally called "the electrical wall." Let the surface impedances of electrical and magnetic walls be designated as $Z_{\text{sur}}^{\text{electr}}$ and $Z_{\text{sur}}^{\text{magn}}$, respectively. It then follows from the aforesaid that

$$Z_{\text{sur}}^{\text{electr}} \ll Z_0 \ll Z_{\text{sur}}^{\text{magn}}. \qquad (26)$$

None of the natural materials offers the properties of the magnetic wall to the full. High-permeability ferromagnets exhibit such properties to an extent. A magnetic wall can be implemented with implicit approaches. Figures 39a and 39b show a structure made up of metallic elements in the form of mushrooms [67]. The structural units of each mushroom are much smaller than the length of a wave incident on this mushroom-formed structure from free space. The equivalent circuit of the loop produced by two adjacent mushrooms is presented in Fig. 39c. The post serves as a lumped inductance, and the gap between caps is a lumped capacitance. This equivalent circuit is identical to that of a cell in the negative-dispersion transmission line (Fig. 8). Each cell of the magnetic wall represents a high-Q resonance circuit ($Q > 100$). The resonance frequency of the circuit depends on the geometrical sizes of the cell and may fall into the range 0.1–100.0 GHz. At a frequency of 16 GHz, experiments with the magnetic wall give the following qualitative estimates: $L = 2$ nH and $C = 0.05$ pF [67]. At resonance frequency $f_0 = 16$ GHz and quality factor $Q = 100$, surface resistance $Z_{\text{sur}}^{\text{magn}}$ is roughly equal to 20 000 Ω and remains fairly high within operating frequency band $\Delta f \cong 0.2$ GHz. It should be immediately emphasized that the artificial magnetic wall retains the "magnetic" properties within a narrow frequency range because of its resonance nature.

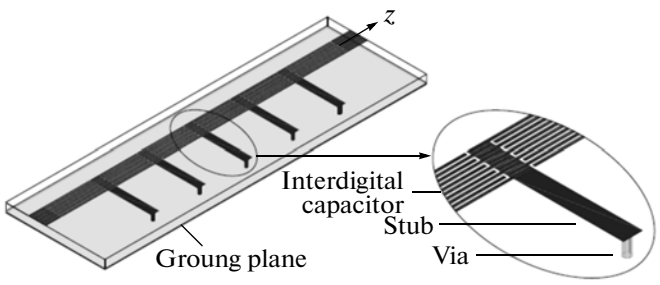

Fig. 33. Transmission line containing series-connected capacitors and parallel-connected short-circuited sections of the transmission lines.

[1] MIMO is a method of data transfer using N transmitting antennas and M receiving antennas. The distances between transmitting antennas and receiving antennas are such that a weak correlation between neighboring antennas is provided.

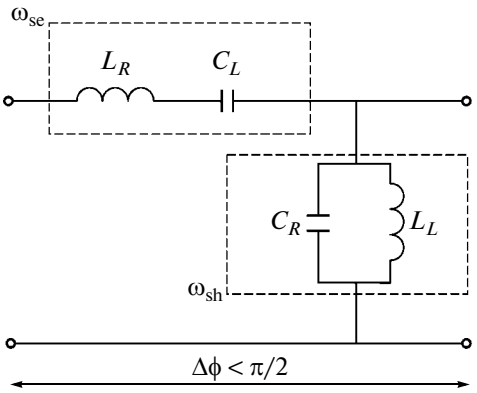

Fig. 34. Equivalent circuit of a unit cell of the transmission line depicted in Fig. 33.

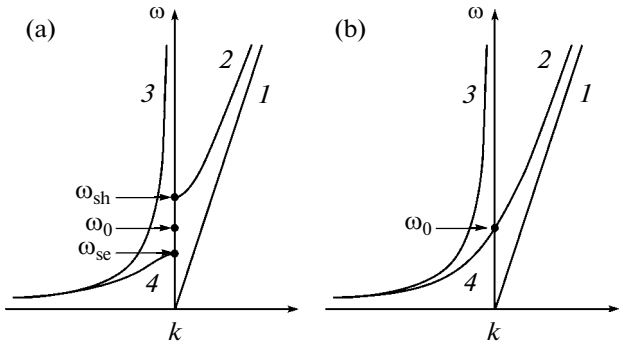

Fig. 35. Dispersion characteristic of the (a) unbalanced and (b) balanced composite transmission line.

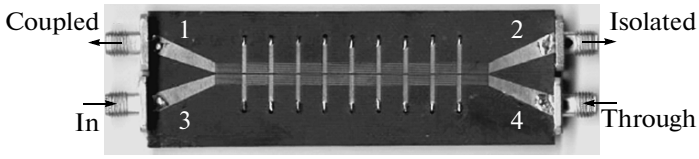

Fig. 36. Photo of the directional coupler consisting of nine cells of the composite transmission line.

Consider briefly how the high-impedance surface (magnetic wall) and the surface of an ideal conductor (perfectly conducting metal) influence the performance of microwave radiators over such surfaces. Figure 40 shows the schematic of a radiator placed parallel to (a) a high-impedance surface and (b) the surface of an ideal conductor (perfectly conducting metal). In both cases, the effect of the surface is akin to that of a current passing through the conductor that is mirror-reflected onto the surface. This current is equivalent to the presence of the second radiator. In the case of the magnetic wall, the current in the reflected conductor is in phase with the current in the primary (real) radiator; in the case of a wall of a perfectly conducting metal, the current in the reflected conductor is out-of-phase to the current in the primary radiator. In the former case, reflection enhances the radiation of the primary radiator, the radiator–wall distance may be rather small. The values of parameters h_0 and h_1 (Fig. 40) are several hundredths of the wavelength. In the latter case, the radiations of two antiphase currents (in the primary radiator and in its reflection image) cancel each other. The radiation of a conductor over the metal surface is active if the distance between the primary radiator and the plane of its reflection is close to quarter-wavelength in free space ($h_2 = 0.25\lambda_0$). The design solution of placing active and passive radiators on a high-impedance surface has been verified many times and is finding application in miniature antennas (see references in [64, 65]). One more feature of a radiator placed on a high-impedance surface merits attention. In this case, the surface current does not penetrate on the back side of the carrier, and backward radiation (i.e., radiation opposite to the main radiation of the antenna) is absent. If the primary radiator is over a perfectly conducting metal, the surface current appears on the back side of the carrier, causing backward radiation. Figure 41 shows the radiation patterns of a solitary radiator above a high-impedance surface and an ideal conductor. It is seen that the backward radiation in the former case is much weaker.

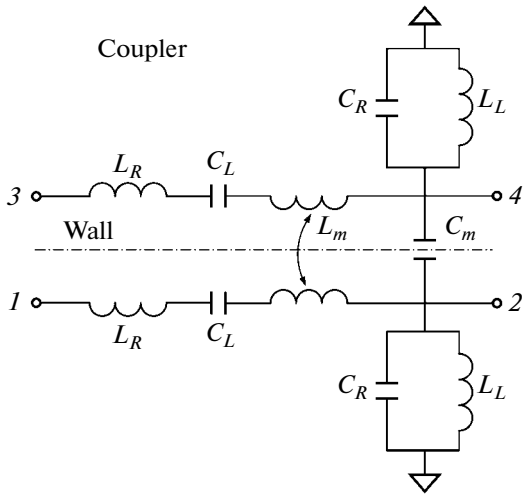

Fig. 37. Equivalent circuit of a cell of coupled composite transmission lines.

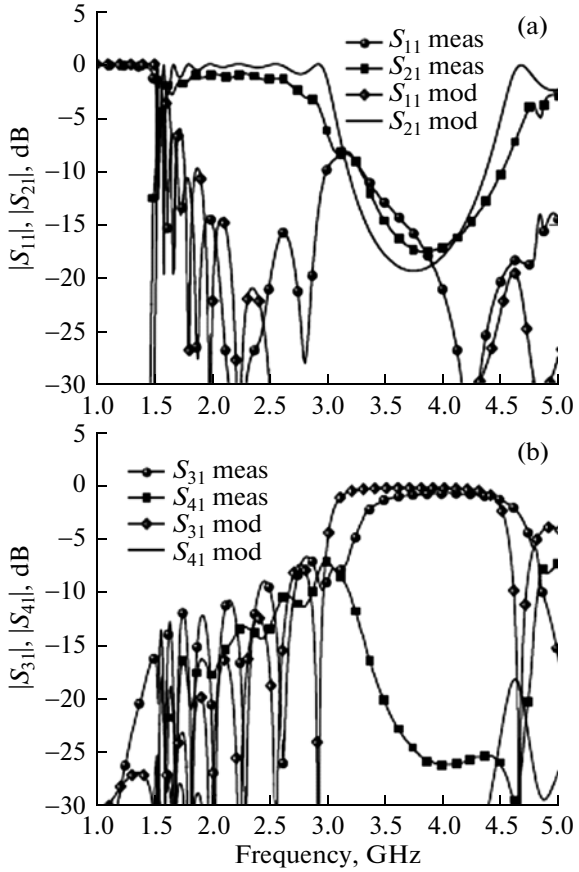

Fig. 38. Calculated and measured parameters (a) S11 and S21 and (b) S31 and S41 of the scattering matrix for the directional coupler built on coupled composite transmission lines.

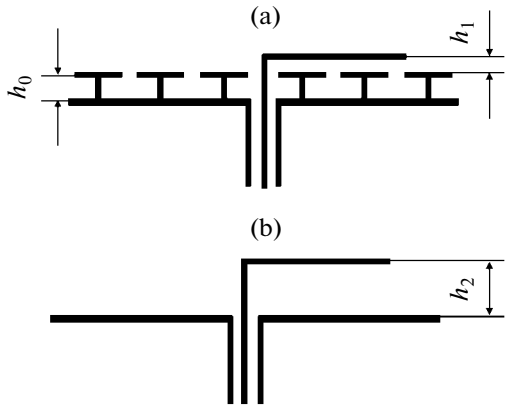

Fig. 40. Horizontal vibrator over the (a) high-impedance surface and (b) high-conductivity metal surface.

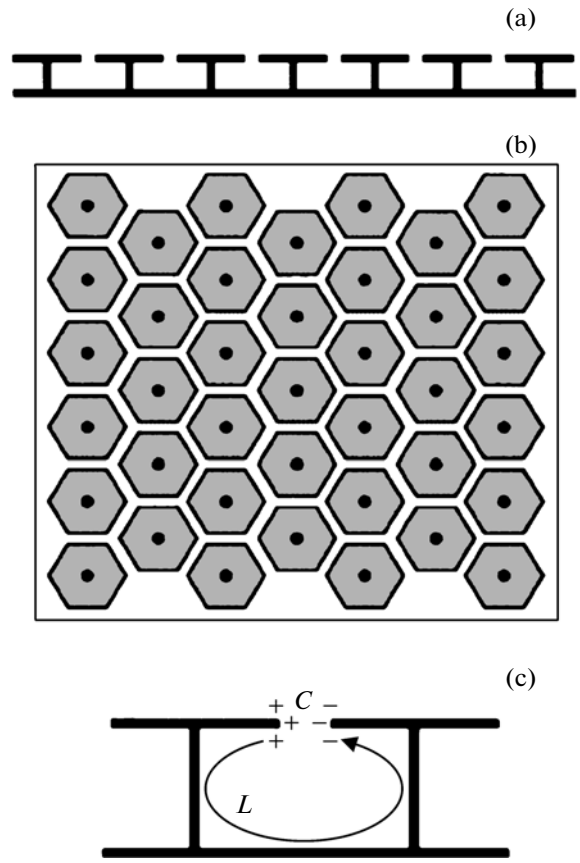

Fig. 39. Embodiment of the high-impedance surface.

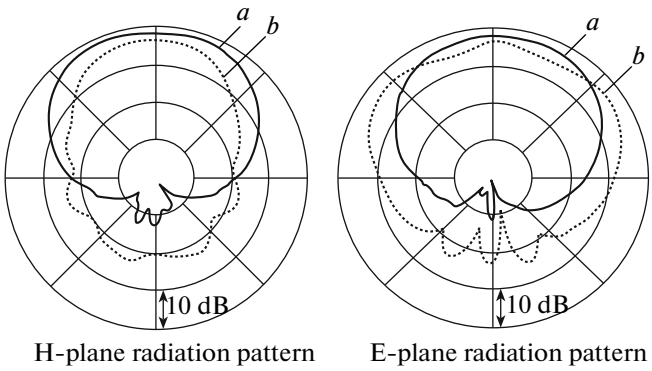

Fig. 41. Radiation patterns in the *E* and *H* planes of the horizontal vibrator over the (a) high-impedance surface and (b) metal surface.

6.2. Surface-Wave Antennas

Metamaterial structures as applied to traveling wave antennas are described at length elsewhere [8, 11]. Figure 42a shows a surface-wave antenna on a composite transmission line. The radiation direction depends on the frequency (Fig. 42b), i.e., is frequency-controlled. At frequency f_0 (point *B* in the figure), the wave radiates normally to the antenna surface; at $f > f_0$, the wave radiates along its propagation direction; and at $f < f_0$, it radiates in the opposite direction. The radiation direction can also be controlled using electrically controlled materials or components entering into the antenna.

Consider a surface-wave antenna with an electrically controlled radiation pattern [68]. Figure 43

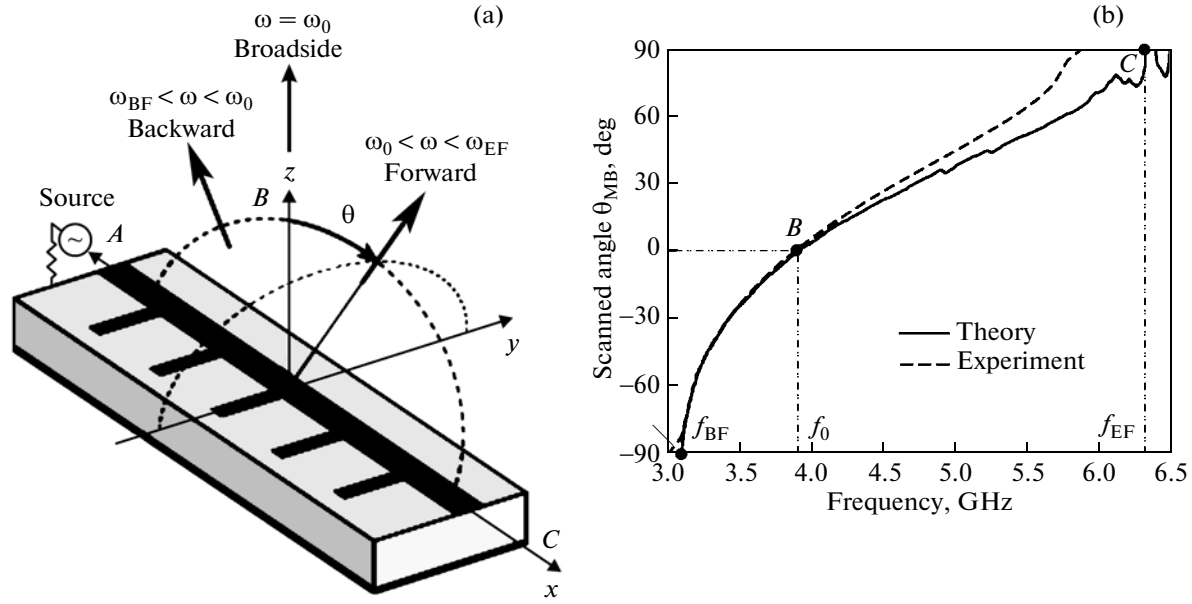

Fig. 42. (a) Surface-wave antenna on the composite transmission line and (b) the dependence of the radiation angle of the antenna on the frequency (i.e., dispersion) of the wave.

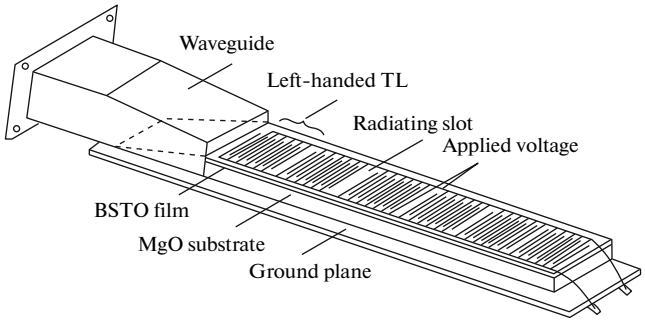

Fig. 43. Design of the surface-wave antenna.

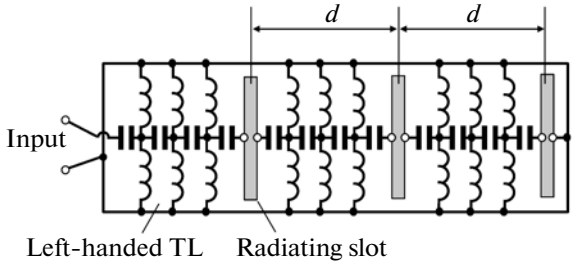

Fig. 44. Electrical circuit of the antenna depicted in Fig. 43.

shows the schematic of a leaky wave antenna representing an array of slot radiators with sections of NDTLs in between. The electrical circuit of the antenna is depicted in Fig. 44. The NDTL sections made in the form of interdigital capacitors are formed by a capacitance between the fingers of the capacitor and an inductance of conductors producing the interdigital capacitor. A wave in the NDTL propagates in such a way that its propagation vector is perpendicular to the fingers of the interdigital capacitor.

The radiation pattern is a superposition of waves radiated by individual slot radiators,

$$F(\theta, \Phi) = \sum_{n=1}^{N} G_0 \exp(-\alpha n) \exp(-ikdn \sin\theta + i\Phi n). \quad (27)$$

Here, G_0 is the gain of the individual slot radiator, α is the damping parameter of the wave in the NDTL, k is the wavenumber in free space, d is the distance between slot radiators, N is the number of slot radiators, Φ is the phase shift of the wave having passed through the NDTL, and θ is the angle within which the radiation of the radiator array is calculated (this angle is measured with respect to the normal to the array).

It is noteworthy that this leaky wave antenna uses a (Ba, Sr)TiO_3 ferroelectric film on which NDTL sections are manufactured. The permittivity of this ferroelectric material considerably depends on the applied bias voltage. The design of a leaky wave antenna using a material with a voltage-controlled permittivity was first suggested in 1982 [68] and then described in detail in 1994 [69]. The thickness of the ferroelectric film is 3.5 μm, and the interfinger gap of the capacitor is 50 μm. Under the a control voltage ranging from 0 to 700 V, the permittivity of the ferroelectric film varies from 1500 to 700. This enables one to significantly change the phase velocity in the NDTL and change the phase shift of the wave after each control element by 0°–180°. A change in the phase shift between adja-

cent slot radiators causes a change in the direction of the main lobe of the radiation pattern. Figure 45 shows the test structure of the antenna intended for a frequency of 37.5 GHz, which corresponds to wavelength $\lambda_0 = 8$ mm in free space. The distance between the slot radiators is $d = \lambda_0/2$. The radiation pattern of the antenna for different control voltages applied to the NDTL electrodes is illustrated in Fig. 46.

In the upper part of Fig. 46, the numbers of beams formed by the antenna array at phase shift $\Phi = 0°$, 45°, 90°, 120°, 150°, and 170° are indicated. In calculations, we put $\alpha = 0.01$ and $N = 8$. The phase shift depends on the capacitance between adjacent elements of the NDTL. When the control voltage varies from 0 to 700 V, the capacitance changes from 0.6 to 0.3 pF. The phase shift versus the capacitance plot is shown in Fig. 47.

6.3. Suppression of the Influence of Antenna Array Elements

It is known that the properties of phased antenna arrays depend on mutual coupling between adjacent radiators in the array [70]. SRR-terminated transmission lines were considered in Section 5. The SRR properties can be used to improve isolation between adjacent radiators in phased array antennas. Figure 48 demonstrates two simple printed radiators that are excited by coaxial lines. At a frequency of 5 GHz ($\lambda_0 =$ 6 cm), the center distance of the radiators is 4 cm. The radiators are separated by an artificial wall containing a set of SRRs (Fig. 48c) and having a high impedance with respect to electromagnetic waves existing around the printed radiators. The transient attenuation between the radiators is 15 dB without the SRR-containing wall and 30 dB in the presence of the wall [66].

Figure 49 shows a simple array of radiators containing 7×3 elements. Rows of three inphase radiators are separated by SRR-containing walls. The main lobe of the antenna has a width of 14°. When the current phase distribution is controlled, the lobe deflects in the E plane by ±30°. Without the wall with SRRs, the antenna "grows blind" at deflection angles of ±19°. At such deflections angles, a surface wave propagates along the radiator array. This wave disturbs matching between the radiators and feed lines, and the antenna gain decreases by 15 dB. In the presence of the SRR-containing wall, such a sharp decrease in the antenna gain is not observed.

Good isolation between closely spaced antennas is of significance in MIMO systems, where one antenna receives and the other transmits signals. Figure 50 shows the layout and characteristics of two MIMO antennas with metamaterial structures in between. From Fig. 50b it follows that the isolation at the point of resonance between metamaterial structures reaches 40 dB.

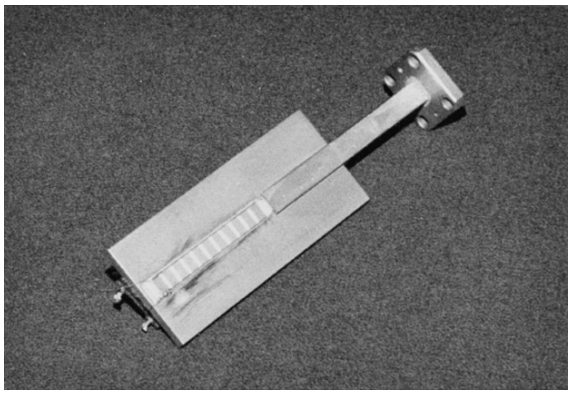

Fig. 45. Photo of the antenna depicted in Fig. 43.

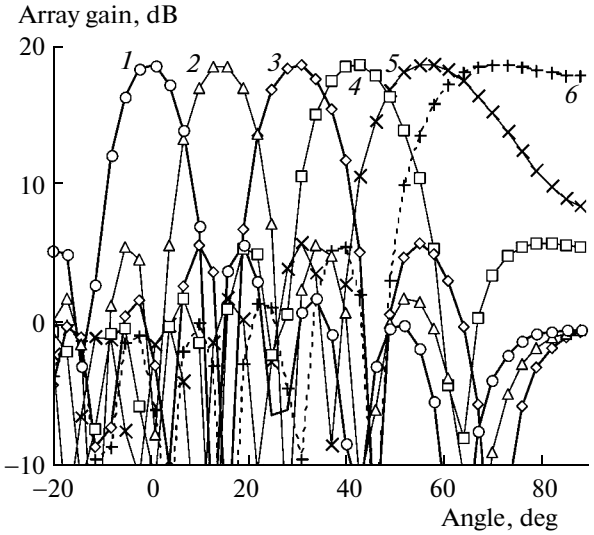

Fig. 46. Variation of the radiation pattern of the surface-wave antenna with phase shift between adjacent slot radiators.

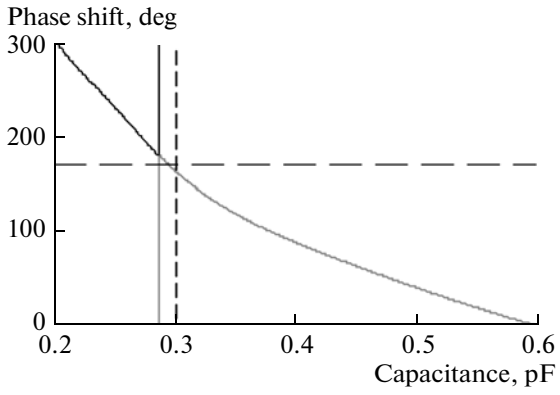

Fig. 47. Phase shift in one phase shifter vs. the capacitance between adjacent elements in the NDTL.

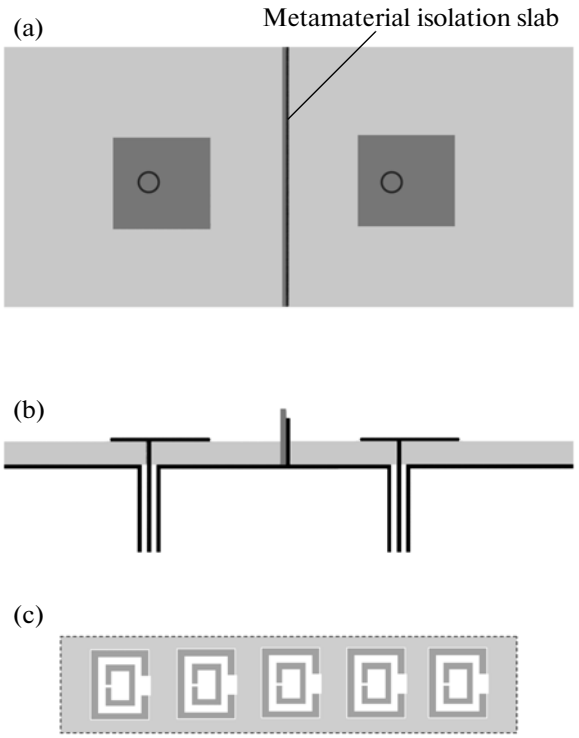

Fig. 48. Simple printed coax-excited radiators. A high-surface-impedance screen (slab) is placed between the radiators.

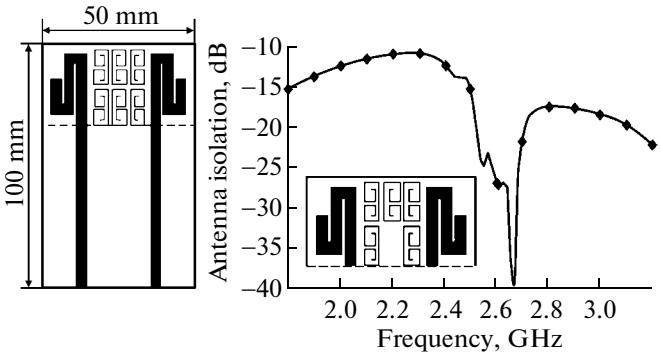

Fig. 50. Layout and characteristics of two antennas incorporated into the MIMO system. The antennas are screened with metamaterial structures.

6.4. Horn Antenna with a Magnetic Wall on the Inner Surfaces

In a conventional horn antenna, an electromagnetic wave obeys boundary conditions on metallic walls. The fundamental mode of the wave is the TE_{01} mode: the electric and magnetic field strengths remain the same along one coordinate and vary by a sinusoidal law along the other coordinate. The efficiency of horn aperture utilization is 50%. In Fig. 51, the field distribution in the cross section of the horn is shown for the case when two walls of the horn are high-impedance

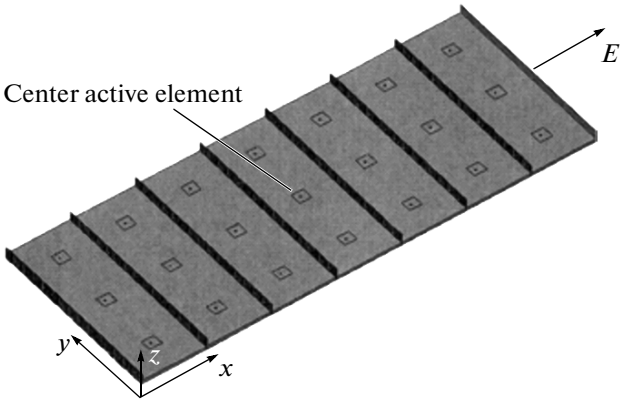

Fig. 49. Phased antenna array in which rows of radiators are screened by the high-surface-impedance slab.

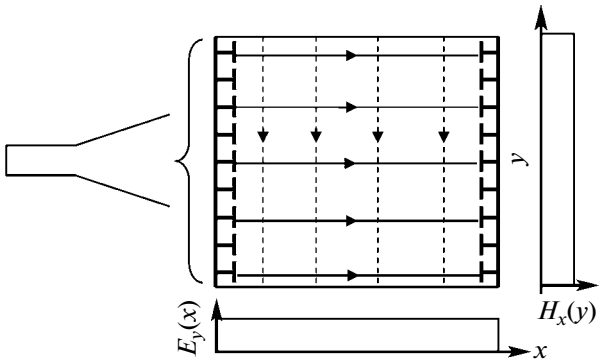

Fig. 51. Field distribution over the cross section of the horn two walls of which serve as high-impedance surfaces.

surfaces. Magnetic lines end on the high-impedance surface, which serves as a magnetic wall. The fundamental mode of the wave in such a horn is the TE_{00} mode: the electric and magnetic field strengths are independent of both coordinates, and the efficiency of horn aperture utilization is 100%.

CONCLUSIONS

This review is based on materials of research performed in a number of European universities and industrial corporations participating in the project of the European Union's framework program FP6 for 2004–2008. The project was titled Metamorphose (MetaMaterials Organized for radio, millimeter wave, and PHOtonicSuperlattice Engineering). The participants of the project were 23 organizations from the leading European countries including St. Petersburg Electrotechnical University "LETI." The financing of the project (4.4 M EURO) was taken care of by the European Commission. From among active participants, the European Commission established in 2005 a nonprofit association "Virtual Institute for Artificial Electromagnetic Materials and Metamaterials"

(Metamorphose VI AISBL).[2] The President of the Virtual Institute is Prof. Sergei Tretyakov, Helsinki University of Technology. "LETI" is also a member of the Virtual Institute. Working at the project and taking part in the activity of the Virtual Institute, we gained much information on the physics of metamaterials and their application in microwave engineering.

The authors of the given review not only worked with European colleagues but also closely communicated with American and Canadian scientists (specifically, with Tatsuo Itoh, University of California, Los Angeles, and Christophe Caloz, École Polytechnique of Montréal) in the framework of international conferences and workshops.

The 6th International Congress on Advanced Electromagnetic Materials in Microwaves and Optics "Metamaterials 2012" was held in St. Petersburg on September 17–22, 2012. The congress was organized by the Virtual Institute in cooperation with St. Petersburg Electrotechnical University "LETI" and St. Petersburg National Research University of Information Technologies, Mechanics, and Optics.

Interest in metamaterials (especially in their application at microwaves) is rapidly growing. Experts from many universities and industrial companies are engaged in R & D work in this area.

ACKNOWLEDGMENTS

The authors are indebted to P. Kapitanova, M. Odit, and D. Kholodnyak for their participation in research on metamaterials and generalization of relevant published data.

REFERENCES

1. V. G. Veselago, Sov. Phys. Usp. **10**, 509 (1967).
2. V. E. Pafomov, Sov. Phys. JETP **5**, 592 (1956); **19**, 1321 (1959).
3. D. V. Sivukhin, Opt. Spectrosc. **3**, 308 (1957).
4. R. A. Silin, Vopr. Radioelektron., Ser. 1, No. 4, 3 (1959); Radiotekh. Elektron. (Moscow) **5**, 688 (1960).
5. V. M. Agranovich and Yu. N. Gartshtein, Phys. Usp. **49**, 1029 (2006).
6. K. Yu. Bliokh and Yu. P. Bliokh, Phys. Usp. **47**, 393 (2004).
7. Yu. V. Gulyaev, A. N. Lagar'kov, and S. A. Nikitov, Vestn. Ross. Akad. Nauk **78**, 438 (2008).
8. *Metamaterials Handbook*, Vol. 1: *Phenomena and Theory of Metamaterials*, Vol. 2: *Applications of Metamaterials*, Ed. by F. Capolino (Taylor, Boca-Raton, 2009).
9. *Negative-Refraction Metamaterials: Fundamental Principles and Applications*, Ed. by G. V. Eleftheriades and K. G. Balmain (Wiley-IEEE, New Jersey, 2005).
10. *Metamaterials: Physics and Engineering Explorations,* Ed. by N. Engheta and R. W. Ziolkowski (Wiley-IEEE, New Jersey, 2006).
11. Ch. Caloz and T. Itoh, *Electromagnetic Metamaterials: Transmission Line Theory and Microwave Applications* (Wiley, New York, 2006).
12. R. Marques, F. Martin, and M. Sorolla, *Metamaterials with Negative Parameters: Theory, Design and Microwave Applications*, Wiley Series in Microwave and Optical Engineering (Wiley-Blackwell, 2008).
13. D. R. Smith, W. J. Padilla, D. C. Vier, S. C. Nemat-Nasser, and S. Schultz, Phys. Rev. Lett. **84**, 4184 (2000).
14. J. B. Pendry, A. J. Holden, W. J. Stewart, and I. Youngs, Phys. Rev. Lett. **76**, 4773 (1996).
15. J. B. Pendry, A. J. Holden, D. J. Robbins, and W. J. Stewart, J. Phys.: Condens. Matter. **10**, 4785 (1998).
16. J. B. Pendry, A. J. Holden, D. J. Robbins, and W. J. Stewart, IEEE Trans. Microwave Theory Tech. **47**, 1075 (1999).
17. R. A. Shelby, D. R. Smith, and S. Schultz, Science **292**, 77 (2001).
18. O. G. Vendik and M. S. Gashinova, in *Proceedings of the 34th European Microwave Conference, Amsterdam, 2004*, pp. 1209–1212.
19. I. B. Vendik, O. G. Vendik, and M. S. Gashinova, Tech. Phys. Lett. **32**, 429 (2006).
20. I. B. Vendik, O. G. Vendik, I. A. Kolmakov, and M. A. Odit, Opto-Electron. Rev. **14**, 179 (2006).
21. I. Vendik, O. Vendik, and M. Odit, Microwave Opt. Technol. Lett. **48**, 2553 (2006).
22. I. B. Vendik, O. G. Vendik, and M. A. Odit, Phys. Solid State **51**, 1590 (2009).
23. I. B. Vendik, O. G. Vendik, and M. A. Odit, *Theory and Phenomena of Metamaterials: Metamaterial Handbook,* Ed. by F. Cappolino (Taylor, 2009), pp. 21-1–21-32.
24. M. A. Odit, I. B. Vendik, and O. G. Vendik, Izv. St. Peterburg. Gos. Elektrotekh. Univ., No. 7, 3 (2008).
25. I. B. Vendik, M. A. Odit, and D. S. Kozlov, Metamaterials **3** (3–4), 140 (2009).
26. I. Vendik, M. Odit, and D. Kozlov, Radioengineering: Proc. Czech. Slovak. Technol. Univ. URSI Committee **18**, 111 (2009).
27. I. Vendik, M. Odit, and D. Kozlov, *Selected Topics in Photonic Crystals and Metamaterials*, Ed. by A. Andreone, A. Cusano, A. Cutolo, and V. Galdi (World Sci., 2011), Chap. 6, pp. 195–214.
28. C. Holloway and E. Kuester, IEEE Trans. Antennas Propag. **51**, 2596 (2003).
29. A. Ahmadi and H. Mosallaei, Phys. Rev. B **77**, 045104 (2008).
30. T. Ueda, A. Lail, and T. Itoh, in *Proceedings of the 36th European Microwave Conference (EuMC36), 2005*, pp. 435–438.
31. E. A. Semouchkina, G. B. Semouchkin, M. Lanagan, and C. A. Randall, IEEE Trans. Microwave Theory Tech. **53**, 1477 (2005).
32. Q. Zhao, L. Kang, B. Du, H. Zhao, Q. Xie, X. Huang, B. Li, J. Zhou, and L. Li, Phys. Rev. Lett. **101**, 027402 (2008).

[2] The Association has an operational office in Finland at METAMORPHOSE VI Dept. of Radio Science and Engineering, Aalto University, School of Electrical Engineering, PO Box 13000, FI-00076 Aalto, Finland.

33. K. Shibuya, K. Takano, N. Matsumoto, K. Izumi, H. Miyazaki, Y. Jimba, and M. Hangyo, in *Proceedings of the 2nd International Congress on Advanced Electromagnetic Materials in Microwaves and Optics, Pamplona, 2008*, pp. 777–779.

34. X. Cai, R. Zhu, and G. Hu, Metamaterials **2**, 220 (2008).

35. J. D. Baena, L. Jelinek, R. Marques, and J. Zehentner, Appl. Phys. Lett. **88**, 134108 (2006).

36. C. R. Simovski and S. He, Phys. Lett. A **311**, 254 (2003).

37. Th. Koschny, L. Zhang, and C. M. Soukoulis, Phys. Rev. B **71**, 121103 (2005).

38. I. Vendik, D. Kholodnyak, I. Kolmakova, E. Serebryakova, and P. Kapitanova, Microwave Opt. Technol. Lett. **48**, 2632 (2006).

39. I. Vendik, D. Kholodnyak, E. Serebryakova, and P. Kapitanova, Eur. Phys. J.: Appl. Phys. **46**, 45 (2009).

40. V. M. Karpov, V. A. Malyshev, and I. V. Perevoshchikov, *Broadband Microwave Devices on Elements with Concentrated Parameters* (Radio i Svyaz', Moscow, 1984).

41. K. C. Gupta, R. Garg, and R. Chadha, *Computer-Aided Design of Microwave Circuit* (Artech House, London, 1981; Radio i Svyaz', Moscow, 1987).

42. P. V. Kapitanova, A. V. Simin, and D. V. Kholodnyak, Izv. Vyssh. Uchebn. Zaved., Radiofiz., No. 1, 75 (2005).

43. P. V. Kapitanova, A. V. Simine, D. V. Kholodnyak, and I. B. Vendik, J. Eur. Ceram. Soc., No. 27, 2941 (2007).

44. P. V. Kapitanova, A. V. Simine, D. V. Kholodnyak, and I. B. Vendik, in *Proceedings of the 35th European Microwave Conference, Paris, 2005*, pp. 389–392.

45. I. B. Vendik, D. V. Kholodnyak, I. V. Kolmakova, E. V. Serebryakova, P. V. Kapitanova, F. Martin, J. Bonache, J. Garcia, I. Gil, and M. Gil, in *Proceedings of the 36th European Microwave Conference, Manchester, 2006*, pp. 955–958.

46. I. B. Vendik, D. V. Kholodnyak, I. V. Kolmakova, E. V. Serebryakova, and P. V. Kapitanova, Microwave Opt. Technol. Lett. **48**, 2632 (2006).

47. R. Perrone, J. Müller, P. Kapitanova, D. Holodnyak, I. Vendik, S. Humbla, and M. Hein, in *Proceedings of the 17th European Microelectronics and Packaging Conference, Rimini, Italy, 2009*, NEMPC156.

48. D. Kholodnyak, P. Kapitanova, and I. Vendik, in *Proceedings of the 1st International Congress on Advanced Electromagnetic Materials in Microwaves and Optics, Rome, 2007*, pp. 91–94.

49. V. Piatnitsa, D. Kholodnyak, P. Kapitanova, I. Fischuk, T. Tick, J. Jantti, H. Jantunen, and I. Vendik, in *Proceedings of the 37th European Microwave Conference, Munich, Germany, 2007*, p. 636–639.

50. D. Kholodnyak, P. Kapitanova, I. Vendik, S. Humbla, R. Perrone, J. Müller, and M. A. Hein, in *Proceedings of the 38th European Microwave Conference Amsterdam, 2008*, pp. 341–344.

51. I. Vendik, D. Kholodnyak, E. Serebryakova, and P. Kapitanova, Eur. Phys. J.: Appl. Phys. **46**, 32610 (2009).

52. P. Turalchuk, I. Munina, P. Kapitanova, D. Kholodnyak, D. Stöpel, S. Humbla, J. Müller, M. A. Hein, and I. Vendik, in *Proceedings of the 40th European Microwave Conference, Paris, France, 2010*, pp. 1162–1165.

53. L. Brillouin and M. Parodi, *Wave Propagation in Periodic Structures* (Dover, New York, 1953; IL, Moscow, 1959), translated from French.

54. I. Vendik, D. Kholodnyak, P. Kapitanova, et al., in *Proceedings of the 38th European Microwave Conference, Amsterdam, 2008*, pp. 273–276.

55. I. Vendik, D. Kholodnyak, P. Kapitanova, and K. Zemlyakov, in *Proceedings of the 3rd International Congress on Advanced Electromagnetic Materials in Microwaves and Optics, London, 2009*, pp. 591–593.

56. P. Kapitanova, D. Kholodnyak, S. Humbla, R. Perrone, J. Müller, M. A. Hein, and I. Vendik, Microwave Opt. Technol. Lett. **51**, 629 (2009).

57. P. Kapitanova, D. Kholodnyak, S. Humbla, R. Perrone, J. Müller, M. A. Hein, and I. Vendik, Int. J. Microwave Wireless Technol. **1**, 323 (2009).

58. I. B. Vendik, O. G. Vendik, D. V. Kholodnyak, E. V. Serebryakova, and P. V. Kapitanova, Proc. Eur. Microwave Assoc. **2** (2), 30 (2006).

59. D. V. Kholodnyak, E. V. Serebryakova, I. B. Vendik, and O. G. Vendik, IEEE Microwave Wireless Comp. Lett. **16**, 258 (2006).

60. E. Serebryakova, D. Kholodnyak, and I. Vendik, in *Proceedings of the 51th Internationales Wissenschaftliches Kolloquium, Ilmenau, Germany, 2006*, pp. 261–262.

61. A. Lai, C. Caloz, and T. Itoh, IEEE Microwave Mag. **5** (3), 34 (2004).

62. C. Caloz, A. Sanada, and T. Itoh, IEEE Trans. Microwave Theory Tech. **52**, 980 (2004).

63. R. Mongia, I. Bahl, and P. Bhartia, *RF and Microwave Coupled-Line Circuits* (Artech House, Norwood, 1999).

64. V. Slyusar, Elektronika NTB, No. 7, 70 (2009).

65. V. Slyusar, Pervaya Milya, Nos. 3–4, 44 (2010).

66. M. C. Tang, S. Xiao, B. Wang, J. Guan, and T. Deng, IEEE Antennas Propag. Mag. **53** (6), 31 (2011).

67. D. Sievenpiper, L. Zhang, R. Broas, N. G. Alexopolous, and E. Yablonovitch, IEEE Trans. Microwave Theory Tech. **47**, 2059 (1999).

68. O. G. Vendik, I. G. Mironenko, and L. V. Ryzhkova, Radiotekh. Elektron. (Moscow) **27**, 1653 (1982).

69. O. G. Vendik, I. G. Mironenko, and L. T. Ter-Martirosyan, Microwaves RF **33** (7), 67 (1994).

70. O. G. Vendik and M. D. Parnes, *Antennas with Electric Scanning: Introduction to Theory,* Ed. by L. D. Bakhrakh (SAINS-PRESS, Moscow, 2002).